

An excitable Rho GTPase signaling network generates dynamic subcellular contraction patterns

Melanie Graessl,^{1*} Johannes Koch,^{1*} Abram Calderon,² Dominic Kamps,^{1,2} Soumya Banerjee,² Tomáš Mazel,² Nina Schulze,¹ Jana Kathrin Jungkurth,^{1,2} Rutuja Patwardhan,¹ Djamschid Solouk,² Nico Hampe,³ Bernd Hoffmann,³ Leif Dehmelt,^{2,3**} and Perihan Nalbant^{1***}

¹Department of Molecular Cell Biology, Center for Medical Biotechnology, University of Duisburg-Essen, Essen, Germany

²Department of Systemic Cell Biology, Max Planck Institute of Molecular Physiology and Fakultät für Chemie und Chemische Biologie, TU Dortmund University, Dortmund, Germany

³Institute of Complex Systems, Forschungszentrum Jülich, Jülich, Germany

Rho GTPase-based signaling networks control cellular dynamics by coordinating protrusions and retractions in space and time. Here, we reveal a signaling network that generates pulses and propagating waves of cell contractions. These dynamic patterns emerge via self-organization from an activator–inhibitor network, in which the small GTPase Rho amplifies its activity by recruiting its activator, the guanine nucleotide exchange factor GEF-H1. Rho also inhibits itself by local recruitment of actomyosin and the associated RhoGAP Myo9b. This network structure enables spontaneous, self-limiting patterns of subcellular contractility that can explore mechanical cues in the extracellular environment. Indeed, actomyosin pulse frequency in cells is altered by matrix elasticity, showing that coupling of contractility pulses to environmental deformations modulates network dynamics. Thus, our study reveals a mechanism that integrates intracellular biochemical and extracellular mechanical signals into subcellular activity patterns to control cellular contractility dynamics.

Introduction

The plasma membrane of higher eukaryotic cells serves as a platform for transmitting and processing extracellular and intracellular information (Grecco et al., 2011). In addition, the plasma membrane and the associated cell cortex can also act as an excitable medium capable of lateral signal propagation (Iglesias and Devreotes, 2012; Wu et al., 2013; Bement et al., 2015; Barnhart et al., 2017; Miao et al., 2017; van Haastert et al., 2017). The underlying network architecture of a typical excitable medium is based on a component that controls its own activity by coupled self-amplifying and self-inhibiting mechanisms (Murray, 2002; Iglesias and Devreotes, 2012). A time delay in the self-inhibiting mechanism makes such systems more robust with regard to kinetic parameters of the underlying signaling network (Stricker et al., 2008). If an excitable system is stimulated above a certain threshold, it generates a maximal response followed by an insensitive, refractory period. With spatial coupling, for example via diffusion, such systems can generate propagating wave fronts of excited signal activity (Iglesias and Devreotes, 2012).

*M. Graessl and J. Koch contributed equally to this paper.

**L. Dehmelt and P. Nalbant contributed equally to this paper.

Correspondence to Perihan Nalbant: perihan.nalbant@uni-due.de; Leif Dehmelt: leif.dehmelt@mpi-dortmund.mpg.de

Abbreviations used: BAC, bacterial artificial chromosome; GAP, GTPase-activating protein; GBD, GTPase-binding domain; GEF, guanine nucleotide exchange factor; PH, Pleckstrin homology; STICS, spatiotemporal image correlation spectroscopy; TIRF, total internal reflection fluorescence.

Excitable systems are a key element in the development of multicellular organisms and current models of chemotaxis. In this context, signaling networks that are centered on the Rho GTPases RhoA, Rac1, or Cdc42 are thought to serve a role in exploratory processes such as cortical excitability to direct cleavage furrow positioning in mitotic and meiotic oocytes (Bement et al., 2015), cortical instabilities in the actomyosin cortex of the *Caenorhabditis elegans* embryo (Nishikawa et al., 2017), or protrusion dynamics in small migrating cells, including *Dicytostelium discoideum* and neutrophils (Xiong et al., 2010; Iglesias and Devreotes, 2012; Tang et al., 2014; Yang et al., 2016). However, cell migration in larger cell types is thought to be more complex, involving coordinated cell protrusion and contraction (Burnette et al., 2011).

Although several studies show that excitable signal transduction networks can control cell protrusion (Xiong et al., 2010; Iglesias and Devreotes, 2012; Tang et al., 2014; Yang et al., 2016; Barnhart et al., 2017; Miao et al., 2017; van Haastert et al., 2017), the role of excitability in controlling subcellular contractility is less clear. In nonmuscle cells, cell contraction is driven by actomyosin dynamics downstream of a signal pathway, including the small GTPase RhoA, Rho kinase 1 (ROCK1)

© 2017 Graessl et al. This article is distributed under the terms of an Attribution-Noncommercial-Share Alike-No Mirror Sites license for the first six months after the publication date (see <http://www.rupress.org/terms/>). After six months it is available under a Creative Commons License (Attribution-Noncommercial-Share Alike 4.0 International license, as described at <https://creativecommons.org/licenses/by-nc-sa/4.0/>).



and ROCK2, and myosin light chain kinase/phosphatase (Riento and Ridley, 2003). Rho is thought to be key to the spatiotemporal regulation of this pathway. However, Rho activity is also known to stimulate actin polymerization via other effectors, including formins of the diaphanous family (Kühn and Geyer, 2014). Because of the influence of Rho activity on multiple distinct cellular processes, the analysis of bulk Rho activity alone is not sufficient to untangle its cellular functions.

Here, we focus on the role of Rho in regulating contraction in adherent cells by simultaneous imaging of endogenous Rho activity and Myosin II dynamics. Using this strategy, we uncovered spontaneous, subcellular pulses and propagating waves of Rho activity that are coupled to subcellular patterns of Myosin II localization and actomyosin contraction.

Our analysis of the connectivity between these components and regulatory factors reveals an activator-inhibitor network, in which Rho self-amplification via the guanine nucleotide exchange factor (GEF) GEF-H1 (ARHGEF2) is coupled to Rho inhibition via delayed activation and accumulation of actomyosin and the associated RhoGAP Myo9b. Our experimental manipulations show that this signaling network is critical for the spontaneous emergence of pulses and propagating waves of Rho activity. Furthermore, we show that network dynamics are modulated by the expression level of associated regulators and the elasticity of the extracellular matrix to control cell contractility dynamics.

Results

Local Rho activity pulses in cultured adherent cells

In a previous study, we found that the Rho effectors FHOD1 and nonmuscle myosin heavy chain IIa (Myosin IIa, MYH9) accumulate near the leading edge of spreading U2OS cells to cooperate in the generation of a subpopulation of stress fibers called actin arcs (Schulze et al., 2014). During cell protrusion, such stress fibers are thought to form a structural basis to couple substrate adhesion and extension of the cells' leading edge via actin polymerization (Burnette et al., 2011). Here, we found that in addition to this expected localization, spontaneous pulses of Myosin IIa association with the cortical actin cytoskeleton occur near the cell center. To investigate the signaling network that controls these patterns, we combined measurements of effector plasma membrane association with activity measurements of Rho itself. We used a fluorescent protein fusion of the GTPase-binding domain (GBD) of the Rho effector Rhotekin as a Rho activity sensor (Benink and Bement, 2005). This domain was shown to bind specifically to the active form of the related GTPases RhoA, RhoB, and RhoC (collectively termed Rho in this article) but neither to inactive Rho nor to active Rac1 or Cdc42 (Reid et al., 1996; Ren et al., 1999). We used total internal reflection fluorescence (TIRF) microscopy to measure the recruitment of the Rhotekin GBD to local areas of increased endogenous Rho activity at the plasma membrane. To reduce potential competition between the sensor and endogenous effectors, we expressed Rhotekin-GBD under the control of the very weak delCMV promoter (Watanabe and Mitchison, 2002). To quantify spatiotemporal activity patterns, we developed custom-built ImageJ macros to measure several parameters, including the standard deviation of the local signal intensity (see Materials and methods).

Using this strategy, we observed highly dynamic, local pulses of Rho activity (Fig. 1, a–f; and Video 1, top). Interestingly, these dynamic patterns were detected in resting, adherent cells, which were neither stimulated nor perturbed by pharmacological compounds. These dynamic changes in signal intensity were not observed in cells expressing only the fluorescent protein, which was used as a soluble control sensor (Fig. 1, b and c; and Fig. S1, a and b). To test whether signal pulses detected with the Rhotekin-GBD sensor might be caused by membrane movement in and out of the TIRF field, we also included an additional, membrane-anchored control sensor that consists of the fluorescent protein, coupled to the C-terminal targeting sequence of K-Ras (EGFP-CAAX). Neither the soluble nor the membrane-anchored control sensor displayed local pulses in their signal (Fig. S1, a–d). Furthermore, small changes in soluble and membrane-anchored control sensor signal did not correlate with signal changes of the Rhotekin-GBD sensor, clearly showing that Rhotekin-GBD signal changes do not derive from movements of the plasma membrane (Fig. S1, a–d). Pixel-based spatiotemporal autocorrelation analysis revealed that spontaneous Rho activity patterns were focused to small subcellular regions with a decay length of $1.9 \pm 0.3 \mu\text{m}$ and a half-time of $21.7 \pm 4.4 \text{ s}$ (Fig. 1, d–f).

During cell spreading, we also observed dynamic Rho activity changes, as well as occasional, more prominent Rho activity peaks (Fig. S1, e and f, yellow arrow; and Fig. S1 g). These Rho activity peaks were coupled to increased Myosin IIa plasma membrane localization. However, Myosin IIa was distributed in two distinct populations that differed both in their cellular localization and coincidence with increased Rho activity (Fig. S1, e–g). Myosin IIa was either concentrated near the cell edge over time periods of several minutes (Fig. S1 f, magenta arrow) or transiently in more central cell attachment regions (Fig. S1 f, yellow arrow). Only transient myosin cortex associations correlated with increased Rho activity patterns in space and time (Fig. S1, e–g). To quantify the Myosin IIa and Rho sensor signals with respect to the distance between the cell centroid and the cell edge, we transformed cell images of irregular shapes into a normalized, circular shape (Möhl et al., 2012). As shown in Fig. S1 h, the mean intensity of the soluble cytosolic control sensor (EGFP) is nearly equal across the cell attachment area. Mean Rho activity signals are also distributed quite homogeneously, but their change over time as measured by the standard deviation was strongly increased in central cell regions (Fig. S1 i). Mean Myosin IIa signals were maximal near the cell edge; however, temporal signal changes were again predominantly observed in central cell regions.

These analyses thereby confirm the presence of two distinct Myosin IIa populations in spreading cells: a relatively static population of highly concentrated Myosin IIa near the cell edge and a more dynamic population in central regions that overlap with increased Rho activity dynamics (Fig. S1, e–i). Importantly, local Myosin IIa pulses were also detected in resting cells coexpressing fluorescently labeled actin, showing that Myosin IIa cortex association dynamics is independent of the overexpression of the Rho activity sensor (Fig. S1, j and k).

Mechanism of Rho activity self-amplification

We next investigated the source of the observed, spatiotemporal Rho activity dynamics, which included both highly irregular occasional peaks (Fig. 1 b) and more regular, locally recurring activity maxima (Fig. S2 b). Because of this apparent

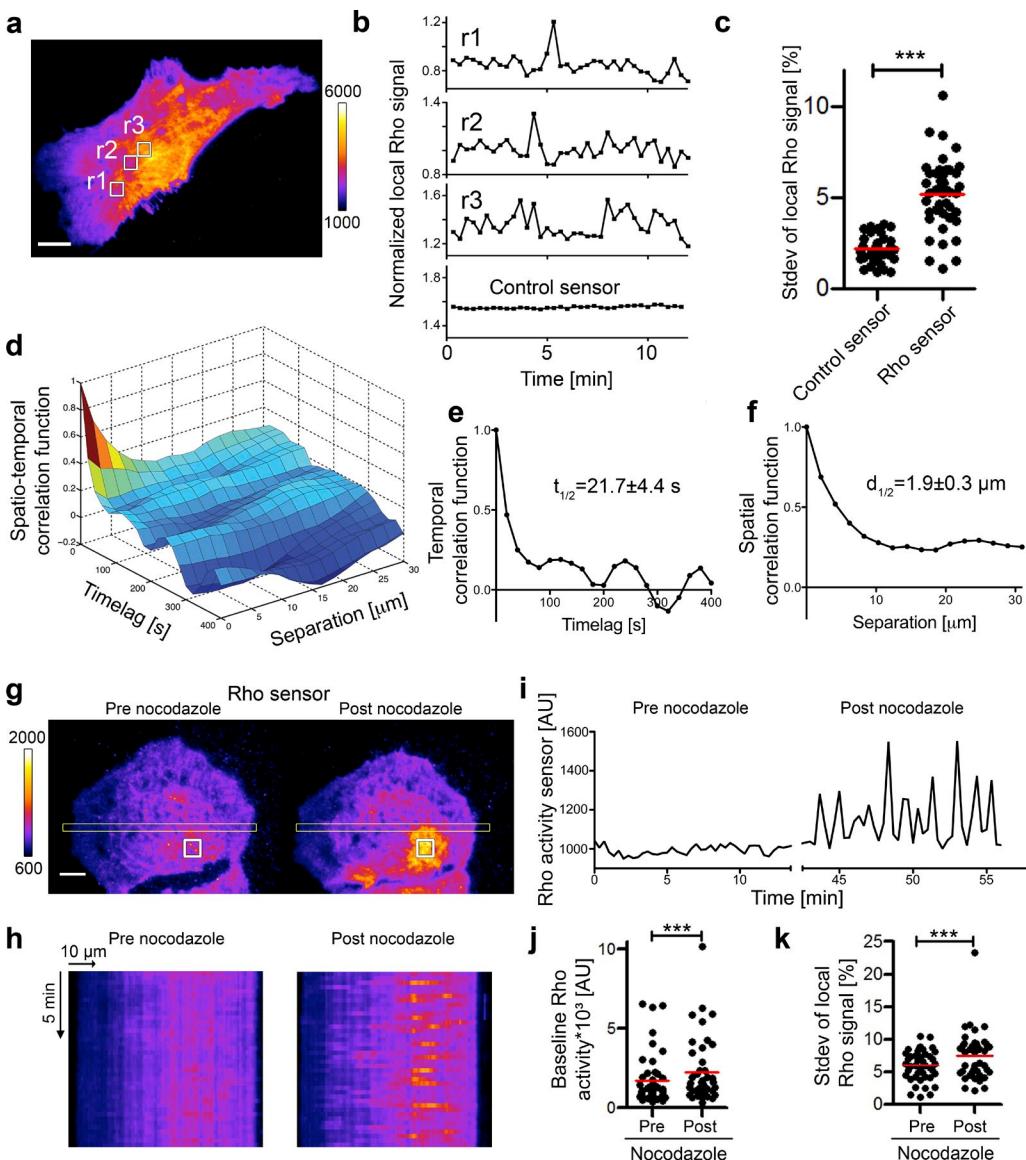


Figure 1. Spontaneous pulses of Rho activity. (a) Representative TIRF image of Rho activity in resting U2OS cells (see also Video 1, top). (b) Local Rho activity dynamics within white boxes in a, normalized to global mean intensity values. No pulses are observed in cells expressing the control sensor (see also Fig. S1, a–d, for direct comparison of raw signal data). (c) Standard deviation of local Rho activity signal dynamics (percentage of mean intensity; $n \geq 37$ cells from three experiments). (d–f) Representative spatiotemporal autocorrelation function derived from the cell shown in panel a. (e and f) Values represent half-time (e) and half-distance (f) \pm SEM ($n = 39$ cells from three experiments). (g–k) Rho activity was stimulated by nocodazole-induced microtubule depolymerization. This induced recurrent local Rho activity pulses with increased amplitude. (g) TIRF images of the Rho activity sensor before and after nocodazole treatment (see also Video 1, bottom). (h) Kymographs corresponding to regions in g (yellow rectangles). (i) Rho activity signal within the white boxes in g. (j and k) Baseline Rho activity (j) and standard deviation of local Rho signal (k; percentage of mean intensity) before and after nocodazole addition ($n = 43$ cells from three experiments). Frame rate is 3/min. Bars, 10 μ m. ***, $P < 0.001$ (c, unpaired t test; j and k, paired t test). For detailed analyses of unperturbed, spreading cells, see Fig. S1 (e–i).

periodicity, we excluded a purely stochastic cause and sought to identify the mechanism that can explain this dynamic behavior. Several distinct network topologies that include a negative feedback are known to generate periodic activity changes (Tyson et al., 2003). A subset of these systems, so-called activator–inhibitor networks, also include a positive feedback (Tyson et al., 2003). This network topology can also form the basis for excitable systems (Iglesias and Devreotes, 2012), such as those that enable the propagation of action potentials in neurons (Fitzhugh, 1961; Nagumo et al., 1962), chemical waves (Winfree, 1984), or of Rho activity in the cortex of oocytes (Bement et al., 2015).

In principle, Rho could either be an integral part of a dynamic signaling network, or it could simply be positioned downstream of a signaling network that generates activity pulses independently of Rho. To investigate the underlying network structure that generates the observed Rho activity dynamics in adherent cells, we introduced an acute, global Rho activity perturbation and measured how this acute perturbation affects Rho activity dynamics.

Microtubule depolymerization is a rapid method that is known to increase Rho activity in cells by releasing the microtubule-bound RhoA activating GEF-H1 (Krendel et al., 2002; Chang et al., 2008). As expected, shortly after application of the

microtubule-depolymerizing drug nocodazole, we observed a significant ($P < 0.001$) increase in Rho activity sensor baseline levels (Fig. 1, g–j; and Fig. S2 a). In addition, we also observed a clear increase in the standard deviation of local Rho activity signals ($P < 0.001$; Fig. 1, i, h, and k; and Video 1, bottom), and we observed propagating Rho activity waves (Fig. S2 c), suggesting that Rho and/or GEF-H1 activity are integral parts of an excitable signal transduction network. Neither the soluble nor the membrane-anchored control sensors showed increased dynamics in the presence of nocodazole (Fig. S2, d–f), further strengthening our previous statement that Rhotekin-GBD signal changes do not derive from movements of the plasma membrane.

Next, we tested whether the Rho activator GEF-H1 might mediate the increase in Rho activity dynamics after nocodazole treatment. Indeed, overexpression of WT or microtubule-binding-deficient C53R mutant was sufficient to increase Rho activity pulse amplitude in the absence of nocodazole (Fig. 2, a and b; and Video 2). In contrast, a GEF-deficient double mutant (C53R, Y393A) had no effect. Furthermore, we frequently observed propagating waves of Rho activity in the presence of GEF-H1 WT ($34.8 \pm 7.4\%$ SEM) and GEF-H1 C53R ($47.4 \pm 8.4\%$ SEM), but not in cells expressing the control construct ($0 \pm 0.0\%$ SEM; $n \geq 55$ cells from four experiments). GEF-H1-mediated waves propagated with a relatively constant velocity of $0.39 \pm 0.14 \mu\text{m/s}$ (GEF-H1 WT) and $0.31 \pm 0.12 \mu\text{m/s}$ (GEF-H1 C53R; Video 3, top; $n = 29$ and $n = 17$ cells from three experiments; mean values \pm standard deviation). In addition to the stimulation of wave propagation, we also frequently observed annihilation of two colliding waves (Fig. S2, g and h). Such spatiotemporal patterns (wave propagation and mutual annihilation of wave fronts) are typically observed in excitable systems that combine both positive and negative feedback regulation (Iglesias and Devreotes, 2012).

Because GEF-H1 is a well-known activator of Rho, we hypothesized that it might play a role in forming a positive feedback to amplify Rho activity within local pulses and propagating waves. To enable such a positive feedback, GEF-H1 not only needs to activate Rho but also needs to be activated by Rho (e.g., by being recruited to areas of increased Rho activity). A recent study indeed showed that the Lbc family of GEFs, which includes GEF-H1, can interact with active RhoA via their Pleckstrin homology (PH) domains (Medina et al., 2013). Interestingly, this interaction surface does not overlap with the interaction between inactive RhoA and the Dbl homology domain of an Lbc GEF family member (Chen et al., 2010). Thus, a GEF that is recruited to active Rho via the PH domain would still be able to activate inactive Rho with its Dbl homology domain. Together, these interactions would be able to close a positive feedback loop to amplify Rho activity (Fig. 2 c). Indeed, cross-correlation analysis showed that GEF-H1 is rapidly recruited to sites of Rho activity, thus enabling mutual stimulation between these components (Fig. 2, d–g; and Video 4). In addition, maximal GEF-H1 accumulation was nearly simultaneous with Rho activation, and on average only shifted slightly ahead by $2.5 \pm 0.7\text{s}$ ($P < 0.001$; one-sample t test for Δt being different from 0 s; value \pm SEM). In contrast, no significant time shift was observed using EGFP as a control (Fig. 2, h–k; and Video 4). We next tested, if the interaction between the GEF-H1 PH domain and active Rho is essential for stimulating Rho activity pulses. To test this, we introduced two point mutations in the PH domain (F539A/I541E) that disrupt a hydrophobic patch that was previously found to be critical for the interaction

between Lbc-type GEFs and active RhoA (Medina et al., 2013). Indeed, this GEF-H1 mutant was unable to stimulate Rho activity patterns (Fig. 2 l).

Furthermore, depletion of GEF-H1 via RNAi showed that GEF-H1 is not only essential for the nocodazole-induced increase in Rho activity dynamics but also required for Rho activity pulses in non-nocodazole-treated, resting cells (Fig. 2, m and n; Video 3, bottom; and Fig. S2, i and j). Both in the absence and presence of nocodazole, Rho activity dynamics were rescued by overexpressing the siRNA-resistant WT GEF-H1, but not using the resistant GEF-H1 construct with the mutated PH domain (F539A/I541E) or the GEF-deficient mutant (Y393A). Thus, GEF activity, as well as the interaction between GEF-H1 and active RhoA, is crucial for the generation of Rho activity dynamics, both in resting cells and after their nocodazole-induced stimulation.

In contrast, overexpression of the Rho GEF Ect2, which does not belong to the Lbc family, only had a small effect on the standard deviation of local Rho activity, and we did not observe any propagating Rho activity waves ($0 \pm 0.0\%$ SEM; Fig. 2 o). The N-terminally truncated, constitutively active mutant Ect2 414–882 stimulated Rho activity dynamics only in a small subset of cells ($21.7 \pm 11.1\%$ SEM; Fig. 2 o, magenta). In contrast to GEF-H1-induced Rho activity waves, which were predominantly localized to central cell regions, waves induced in this subset of Ect2 414–882-expressing cells propagated within the cell periphery (Fig. 2 p). Interestingly, Ect2 414–882 was not enriched at sites of increased Rho activity but was instead excluded from these regions (Fig. 2, p–r). Furthermore, depletion of Ect2 via RNAi did not reduce but instead slightly increased Rho activity dynamics (Fig. 2 s and Fig. S2 k). In contrast, overexpression of another Lbc family GEF, called LARG, stimulated Rho activity pulses that are very similar to those induced by GEF-H1 (Fig. S2, l and m). Together, this shows that in contrast to the Lbc family members GEF-H1 and LARG, Ect2 does not act as a positive feedback mediator to drive Rho activity dynamics.

The active form of RhoA is expected to diffuse much slower in the plasma membrane than the inactive, cytosolic form (Frick et al., 2007). Therefore, RhoA itself might be concentrated within local Rho activity pulses. Indeed, we did observe highly significant local pulses and propagating waves of RhoA plasma membrane association, which closely correlated with the localization of the Rho activity sensor (Fig. S3, a–d). Furthermore, these pulses were stimulated by nocodazole treatment, showing that RhoA can amplify its own local concentration via the GEF-H1-stimulated positive feedback loop (Fig. S3 e). However, in direct comparison, the amplitude of RhoA localization dynamics was lower than the amplitude of Rho activity sensor dynamics. Thus, local Rho activity pulses result from the combination of Rho self-activation and local accumulation, the latter presumably because of the slow diffusion of the active form of Rho.

Spatiotemporal mapping of Rho GTPase signaling

Previous studies suggested that cross talk between Rho GTPases can control their subcellular activity patterns (Benink and Benent, 2005; Machacek et al., 2009; Guilluy et al., 2011). To map the timing of Rac1/Cdc42 activity in relation to Rho activation, we used temporal cross-correlation analysis. In these experiments, we enhanced the sensitivity of our correlation analysis

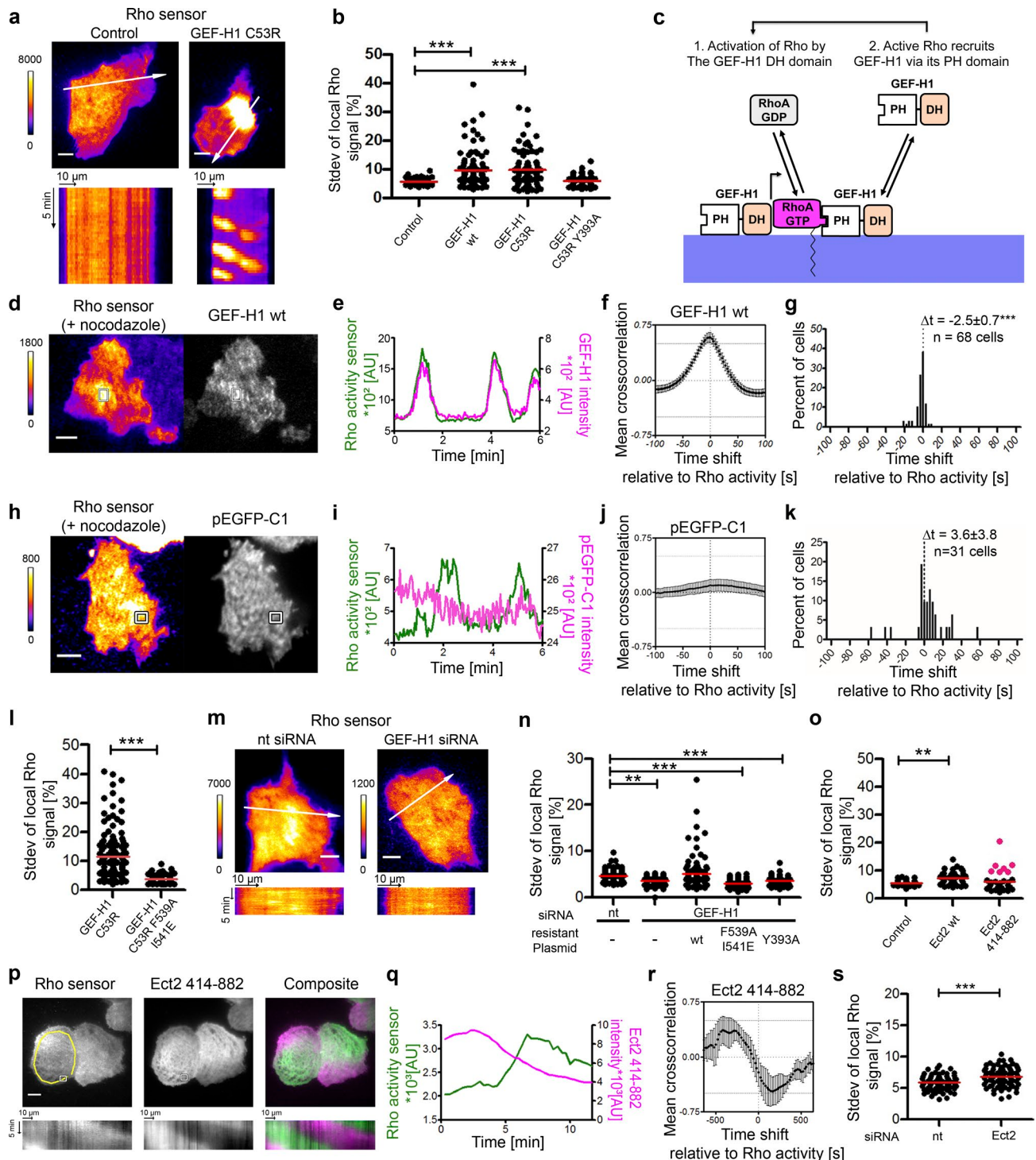


Figure 2. GEF-H1 mediates Rho activity self-amplification. (a) TIRF images of the Rho activity sensor mCherry-Rhotekin-GBD in U2OS cells coexpressing EGFP (control) or EGFP-GEF-H1 C53R (see also Video 2). Kymographs correspond to arrows. (b) Standard deviation of local Rho signal ($n \geq 55$ cells from four experiments). (c) Proposed mechanism of Rho activity amplification via GEF-H1. (d–k) Temporal cross-correlation analysis of the Rho activity sensor mCherry-Rhotekin-GBD and EGFP-GEF-H1 WT (d–g) or EGFP localization (h–k) in nocodazole-treated cells. (d and h) Individual images of TIRF measurements (see also Video 4). (e and i) Intensity measurements from boxes in d and h. (f and j) Temporal cross-correlation functions and frequency distribution (g and k) of cross-correlation maxima derived from f and j ($n \geq 30$ cells from three experiments; error bars represent 95% confidence interval). (l) Standard deviation of local Rho activity signal in cells coexpressing GEF-H1 C53R or GEF-H1 F539A I541E ($n \geq 124$ cells from three experiments). (m) TIRF images of the Rho activity sensor mCherry-Rhotekin-GBD in U2OS cells treated with nontargeting (nt) or GEF-H1 siRNA. Kymographs correspond to arrows (see also Video 3, bottom). (n) Standard deviation of local Rho activity signal in cells treated with nt or GEF-H1 siRNA and coexpressing control (EGFP), siRNA-resistant GEF-H1 WT, siRNA-resistant GEF-H1 F539A I541E, or siRNA-resistant GEF-H1 Y393A ($n \geq 82$ cells from four experiments). (o) Standard deviation of local Rho activity signal in cells coexpressing control (EGFP) or Ect2 constructs ($n \geq 36$ cells from three experiments; measurements from a small subpopulation of cells that show wave propagation are marked in magenta). (p) Representative TIRF images from the subpopulation of cells marked magenta in panel o. Kymographs correspond to yellow circular line. (q) Intensity measurements within the regions indicated by white boxes in panel p. (r) Temporal cross-correlation function for Ect2 414-882. (s) Frequency distribution of cross-correlation maxima for Ect2 414-882. $\Delta t = 1.5 \pm 0.5$ *** $n = 36$ cells.

by stimulating robust Rho activity pulses via nocodazole-induced release of GEF-H1 from microtubules. To measure Rac1 and Cdc42 activity, we used fluorescent protein fusions of the GBDs of the corresponding specific effectors p67^{phox} (NCF2; Lapouge et al., 2000) and WASP (WAS; Symons et al., 1996). The p67^{phox} GBD was not yet used to study Rac1 activity in living cells via TIRF microscopy. We therefore first validated this probe by combining sensor signal measurements with optogenetic switching of Rac1 activity (Fig. S3, f–h). As shown in Fig. S3, i–l (and Video 4), we did not observe altered Rac1 activity within or near Rho activity peaks. Also, in contrast to the expected segregation of Cdc42 and Rho activity (Benink and Bement, 2005; Machacek et al., 2009), we observed that Cdc42 activity largely overlapped with Rho activity peaks with variable delays between their maxima of 0–20 s (Fig. S3, m–p; and Video 4). These results show that neither Rac1 nor Cdc42 activity precedes Rho activity amplification and therefore cannot trigger Rho activity pulses.

Next, we used cross-correlation analyses to study well-characterized cellular functions of Rho activity: stimulation of actin polymerization and myosin activation. We observed strong cross-correlation of Rho activity and actin plasma membrane localization (Fig. 3, a–d; and Video 5, top) with a delay of 11.0 ± 1.1 s ($P < 0.001$; one-sample t test; value \pm SEM). The localization of FHOD1, which is activated by ROCK-mediated phosphorylation downstream of RhoA (Takeya et al., 2008), correlated with Rho activity with a shorter delay of 6.3 ± 0.8 s ($P < 0.001$; one-sample t test; value \pm SEM; Fig. S3, q–t). This suggests that actin nucleation, polymerization or recruitment is stimulated within the cell cortex close to the plasma membrane downstream of Rho activity via effectors such as FHOD1. Furthermore, we observed similar spatiotemporal pulses and propagating waves of FHOD1 in 48.1 ± 18.1 % (SEM) of pluripotent, bacterial artificial chromosome (BAC)-transgenic mouse embryonic stem cells ($n = 57$ cells from five experiments) and spontaneous Rho activity pulses in several types of resting and unstimulated adherent cells (unpublished data), showing that this phenomenon is not limited to transformed U2OS osteosarcoma cells (Fig. S3, u–w). Furthermore, FHOD1 was expressed at low levels under its endogenous promoter in BAC-transgenic mouse embryonic stem cells. Thus, pulses and propagating waves of this Rho effector are independent of additional protein overexpression, in particular concerning signaling network components and associated factors such as the Rho activity sensor or Myosin II.

Interestingly, the association between Myosin IIa and the cell cortex correlated strongly with Rho activity patterns in space and time with a pronounced delay (Fig. 3, e–l; and Video 5, two bottom panels). A similar delay was observed in nocodazole-treated cells (39.5 ± 2.4 s; $P < 0.001$; one-sample t test; value \pm SEM; Fig. 3, e–h) and resting cells that were not treated with nocodazole and did not overexpress GEF-H1 (34.9 ± 2.7 s; $P < 0.001$; one-sample t test; value \pm SEM; Fig. 3, i–l). This pronounced lag indicates the presence of a cellular mechanism that acts as a timer to delay maximal Myosin IIa accumulation downstream of Rho activity. We hypothesized

that this delay might be caused by the relatively slow turnover of Myosin II (Chang and Kumar, 2015) and contractile forces (Vicente-Manzanares et al., 2009), which can generate a cortical flow that slowly transports and further locally concentrates myosin in cells. To test this hypothesis, we sought to determine whether the temporally correlated Rho activity and Myosin IIa cortex association pulses were linked to actomyosin contractile flow. We first measured the temporal evolution of flow fields of Myosin IIa translocation via spatiotemporal image correlation spectroscopy (STICS; see Materials and methods). We then calculated the divergence of these flow fields to identify “sources” that correspond to expansive flow or “sinks” that correspond to contractile flow of the actomyosin cell cortex (Fig. 3, m–o). Interestingly, maximal flow (i.e., inward, negative divergence) preceded maximal Myosin IIa cortex accumulation (Fig. 3 p). Temporal cross-correlation analysis revealed a significant lag of 35.1 ± 3.4 s (SEM) between these events (Fig. 3, q–r). Contractile flow peaks were often associated with roughly circular nodes and were followed by symmetrical Myosin IIa flow toward the node center (Fig. 3, m–o, white boxes between $t = 15$ s and $t = 45$ s). The temporal sequence of events suggests that actomyosin contractile flow indeed contributes to local myosin accumulation (Fig. S4 a).

Mechanism of Rho activity self-inhibition

To support robust activity pulses, the positive feedback that amplifies Rho activity needs to be coupled to a time-delayed negative feedback (Stricker et al., 2008). Because of their significant delays (11.0 ± 1.1 and 39.5 ± 2.4 s; mean values \pm SEM) with respect to Rho activation, actin and Myosin IIa are potential candidates to act as platforms to recruit inhibitors that could shut down Rho activity. Indeed, we observed strong spatio-temporal cross-correlation between Rho activity and localization of inactive mutants of the actin-associated Rho-specific GT-Pase-activating proteins (GAPs) Myo9b (Müller et al., 1997) and p190RhoGAP (ARHGAP35; p190ARhoGAP; Arthur and Burridge, 2001; Fig. 4, a–d; and Fig. S4, b–e). Those inactive mutants have previously been used as proxies to study the localization of their corresponding WT GAPs without disturbing cellular phenotype (van den Boom et al., 2007). Using these mutants we measured significant delays in the plasma membrane association of the GAPs after Rho activity peaks in the range between 2.4 and 3 s, suggesting that they act downstream of Rho activity. It should be noted that our measurement of the delay represents an underestimation caused by the delay of Rho sensor plasma membrane association after Rho activation. We also observed significant cross-correlation using the corresponding WT proteins (Fig. 4, e–h; and Fig. S4, f–i). Interestingly, overexpression of WT, but not GAP-deficient, Myo9b lead to an increase in pulse frequency that was associated with a decrease in peak width (Fig. 4, b, f, i, and j; and Video 6). In cells that express GAP-deficient Myo9b, Rho activity pulses occurred irregularly and were separated by a period of 2–7 min (Fig. 4 b). The corresponding power spectrum therefore only shows a broad maximum at low frequencies (Fig. 4 j). In contrast, cells that express WT Myo9b showed more regular oscillations with

(r) Temporal cross-correlation function from subpopulation of cells marked magenta in panel n ($n = 6$ cells from two experiments; error bars represent 95% confidence interval). (s) Standard deviation of local Rho activity signal in cells treated with control or Ect2 siRNA ($n \geq 75$ cells from three experiments). For representative Western blots of GEF-H1 and Ect2 siRNA knockdown, see Fig. S2 (i and k). Frame rate is 3/min (a, b, and l–s) or 20/min (d–k). Bars, 10 μ m. **, $P < 0.01$; ***, $P < 0.001$ (b, n, and o, analysis of variance, Dunnett’s post-test; g and k, one-sample t test; and l and s, unpaired t test).

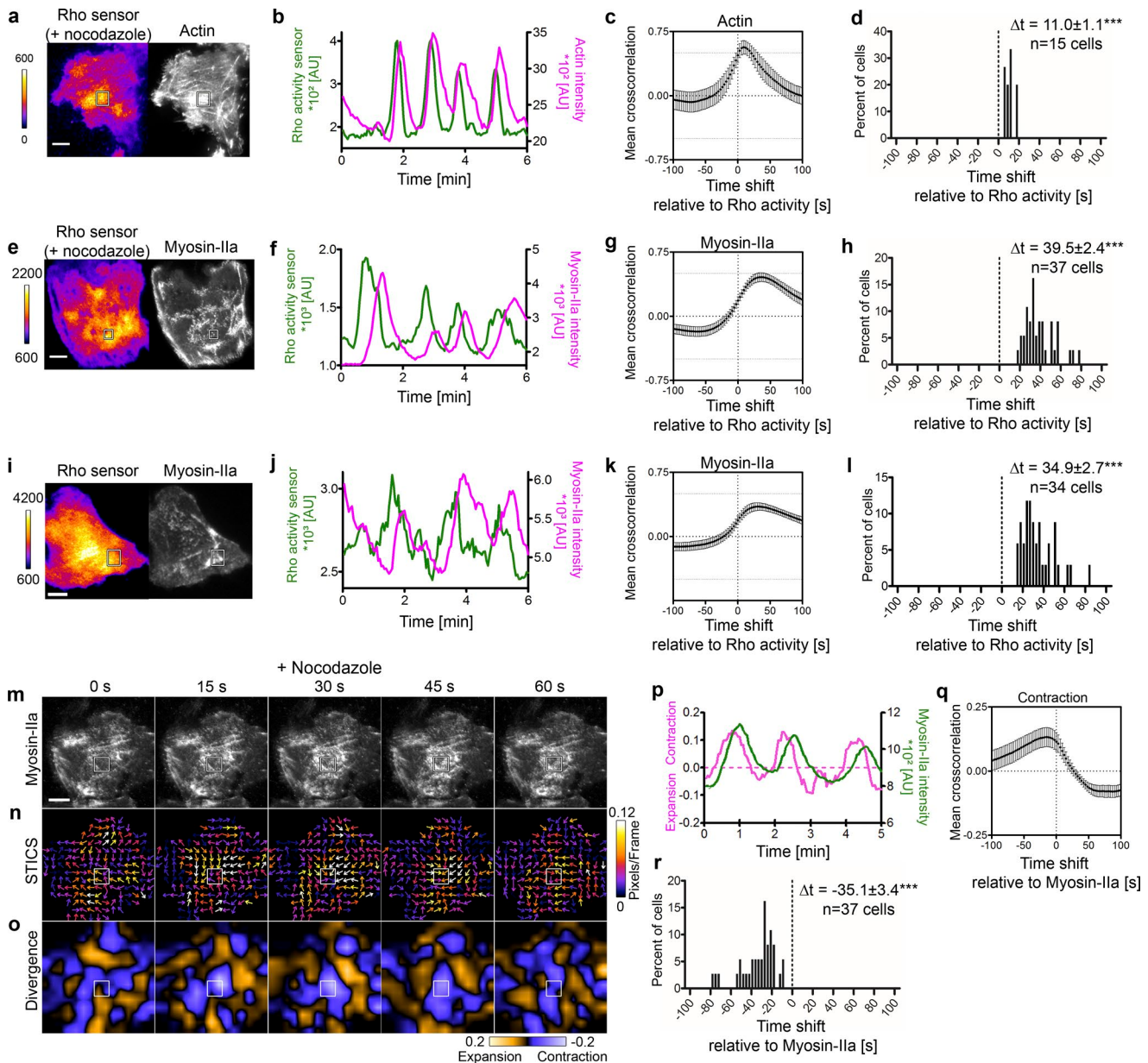


Figure 3. Local Rho activity peaks correlate with actomyosin localization and cell contraction. (a–l) Temporal cross-correlation analysis of the Rho activity sensor mCherry-Rhotekin-GBD and plasma membrane localization of actin (a–d; EGFP-actin; see also Video 5, top), Myosin IIa (e–l; EGFP-NMHCIIa; see also Video 5, middle and bottom). (m–r) Temporal cross-correlation analysis of Myosin IIa signal and contractile flow. Nocodazole-treated (a–h and m–r) or (i–l) untreated, resting U2OS cells. For additional cross-correlation analyses between Rho activity and Rac1, Cdc42, and FHOD1 localization, see Fig. S3. (a, e, i, and m) TIRF images. (n) Color-coded vector fields depicting Myosin IIa flux in m measured via STICS. (o) Contractile and expansive flow of Myosin IIa structures derived from the divergence of the STICS vector map field in panel n. (b, f, j, and p) Intensity or contractile flow measurements within the regions indicated by white boxes in panels a, e, i, m, and o. (r) Temporal cross-correlation functions (c, g, k, and q) and frequency distribution of cross-correlation maxima (d, h, l, and r) derived from panels c, g, k, and q ($n \geq 15$ cells from at least three experiments; error bars represent 95% confidence interval). Frame rate is 20/min. Bars, 10 μ m. ***, P < 0.001 (d, h, l, and r, one-sample t test).

a period of 30–50 s (Fig. 4 f). The corresponding power spectrum therefore contains additional peaks at higher frequencies (Fig. 4 j). The measured delay of WT Myo9b after Rho activity pulses was smaller than that of the GAP mutant, but it was still significant. These observations suggest that Myo9b might act as a mediator of negative feedback; the delayed cross-correlation suggests that it is activated downstream of Rho, and the effect on pulse frequency and peak width suggests that it can also act upstream of Rho to inhibit its activity. In contrast to Myo9b, overexpression of GEF-H1 WT or C53R had the opposite effect

on pulse width (Fig. 4 i). Together, this suggests that the shape of Rho activity peaks is controlled by a balance between activating regulators, such as GEF-H1, that stimulate prolonged Rho activity increase and inhibitory regulators, such as Myo9b, that accelerate subsequent shut down of Rho activity.

These analyses show that Myo9b is able to rapidly shut down Rho activity pulses. In the absence of Myo9b overexpression, additional, slower mechanisms might participate in Rho activity inhibition. Myosin IIa is particularly well suited to mediate such a delayed shut down because of the long delay of

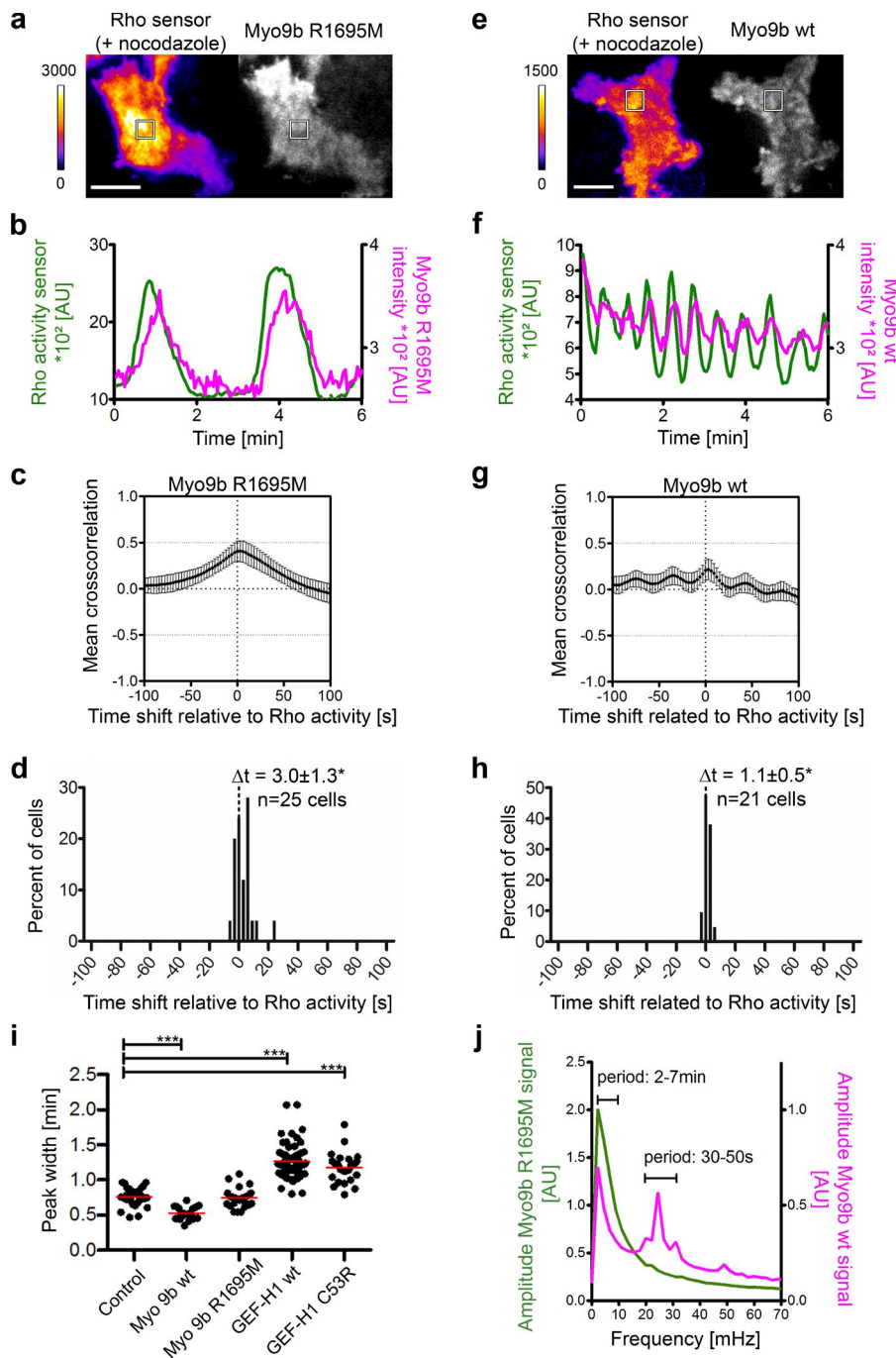


Figure 4. Local Rho activity pulses are modulated by associated GAP and GEF activities. (a–h) Temporal cross-correlation analysis of the Rho activity sensor mCherry-Rhotekin-GBD and RhoGAP Myo9b localization using a GAP-deficient mutant (a–d; R1695M) or WT EGFP fusion proteins (e–h) in nocodazole-treated U2OS cells (see also Video 6). The cross-correlation analyses between Rho activity and p190RhoGAP are shown in Fig. S4. TIRF images (a and e), and intensity measurements (b and f) within the boxes in panels a and e. Temporal cross-correlation functions (c and g) and frequency distribution (d and h) of cross-correlation maxima derived from panels c and g ($n \geq 21$ cells from three experiments; error bars represent 95% confidence interval). (i) Peak width of Rho activity signal ($n \geq 21$ cells from three experiments; red lines represent mean). (j) Fourier analysis of Myo9b WT and R1695M mutant signal intensity ($n \geq 21$ cells from three experiments). Frame rate is 20/min. Bars, 10 μ m. *, $P < 0.05$; ***, $P < 0.001$ (d and h, one-sample t test; i, analysis of variance, Dunnett's post-test).

its accumulation after Rho activation. Indeed, it is known that Myosin IIa can inhibit the activity of Dbl-type GEFs, including GEF-H1 (Lee et al., 2010). In addition, myosin-driven cortical flow (Fig. 3, m–r) could also efficiently concentrate actomyosin-associated RhoGAPs, including Myo9b. Interestingly, GEF-H1 and Myosin IIa overlap in space and time, thereby enabling this inhibitory interaction (Fig. 5, a and b). Furthermore, the onset of GEF-H1 peaks coincided with minimal or decreasing Myosin IIa accumulation (Fig. 5 b), which is reflected in a strong anticorrelation between Myosin IIa and GEF-H1 localization (Fig. 5, c and d). This further supports the idea that Myosin IIa can inhibit GEF-H1 and thus would act both downstream and upstream of Rho activity. If this is the case, then both inhibition of the ROCK that activates Myosin II downstream of RhoA and

direct inhibition of Myosin II activity should interfere with Rho activity pulsing (Figs. 5 e and S5 b). Indeed, if cells were treated with either the Myosin II inhibitor blebbistatin or the ROCK inhibitor Y27632, activity pulses were strongly inhibited (Fig. 5, f–i; Fig. S5; and Video 7). Furthermore, the increased temporal lag between Rho activity pulse peaks after partial inhibition of the Rho–ROCK–Myosin II pathway, as seen in the example shown in Fig. S5 (c–f), suggests that the activity of this pathway acts as a timer to control Rho inactivation. In particular, the last node in this pathway, Myosin II, has a very slow turnover at the cell cortex (Chang and Kumar, 2015). This is in contrast to Myo9b, which turns over at an ~10-fold higher rate (van den Boom et al., 2007). This could also explain the distinct Rho pulse kinetics with or without Myo9b overexpression.

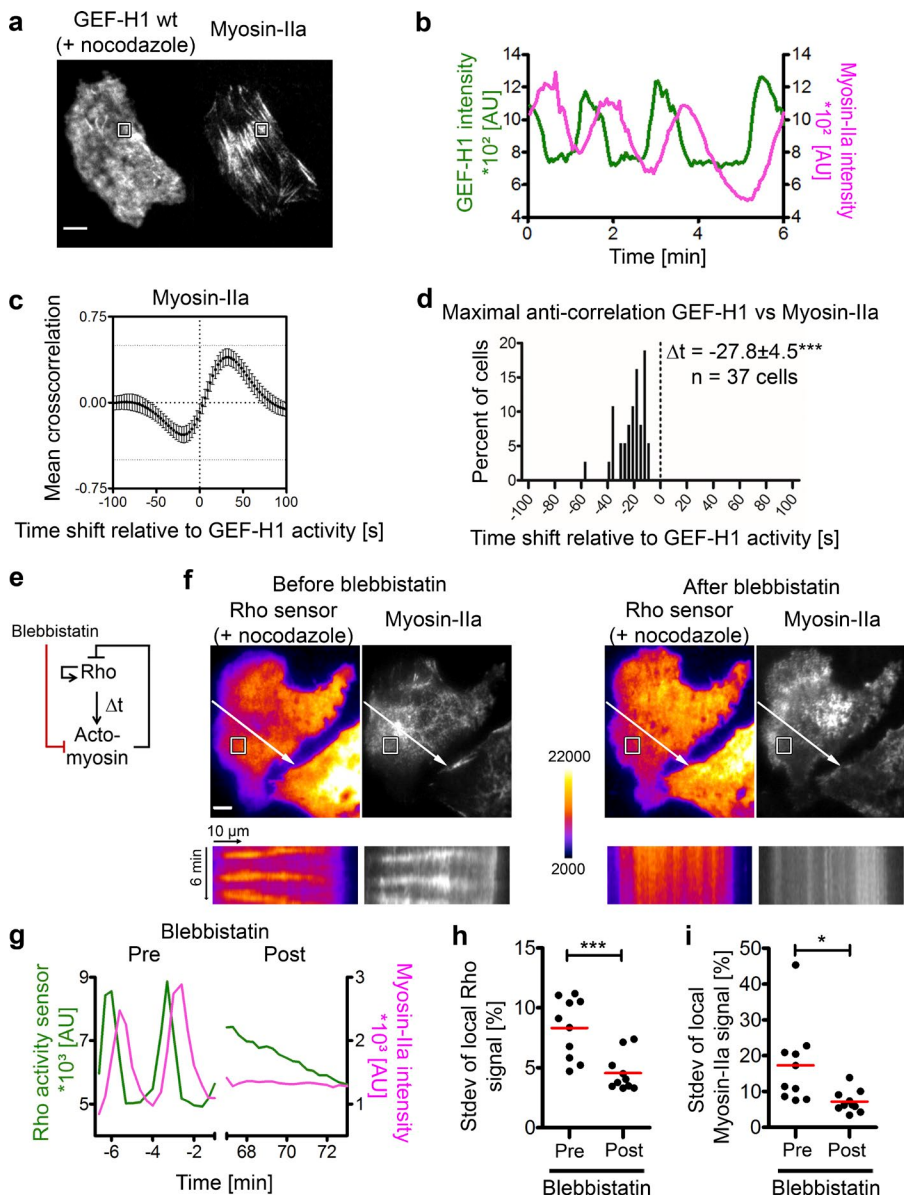


Figure 5. Myosin IIa acts both downstream and upstream of Rho activity patterns. (a-d) Temporal cross-correlation analysis of GEF-H1 (EGFP-GEF-H1 WT) and Myosin IIa (mCherry-NMHCIIa) in nocodazole-treated U2OS cells. (a) Individual images of TIRF measurements. (b) Intensity measurements within white boxes in panel a. (c and d) Temporal cross-correlation functions (c) and frequency distribution (d) of anticorrelation maxima derived from panel c ($n = 37$ cells from three experiments; error bars represent 95% confidence interval). (e) Schematic of the proposed Rho activity based signaling network and inhibition by blebbistatin. The inhibition of ROCK with Y27632 is shown in Fig. S5. (f) TIRF images of the Rho activity sensor mCherry-Rho-kinase-GBD and Myosin IIa (EGFP-NMHCIIa) before and after 50 μ M blebbistatin treatment (1 h; see also Video 7). Kymographs correspond to the white lines in the images above. (g) Intensity measurements within white regions indicated in f. (h and i) Standard deviation of local Rho activity and myosin signal ($n \geq 10$ cells from three experiments; see Fig. S5 a for vehicle controls). Frame rate is 20/min (a-d) or 3/min (f-i). Bars, 10 μ m. *, $P < 0.05$; ***, $P < 0.001$ (d, one-sample t test; h and i, paired t test).

In our experiments, high-amplitude Rho activity pulses always induced high-amplitude myosin peaks, which were associated with clearly detectable contractile flow. However, presumably because of the slow turnover kinetics, the Myosin IIa signal often accumulated over the course of several weaker and shorter pulses and was not always associated with individual, very weak Rho activity peaks. It is thus possible that the GAP activity of actin-associated regulators such as Myo9b might be sufficient to mediate negative feedback in these short Rho activity peaks with small amplitude. Collectively, our analyses reveal multiple actomyosin-associated pathways that can mediate negative feedback regulation of Rho activity at distinct timescales.

Rho activity pulses are coupled to matrix elasticity

Our experiments show that Rho cooperates with its own activator, GEF-H1, to form a positive feedback that is combined with a delayed negative feedback via recruiting the Rho/GEF-H1 inhibitors Myo9b and Myosin IIa. In combination, these feedbacks act on the scale of molecules to form a self-organizing system that is

capable of spontaneously generating spatiotemporal activity patterns. Interestingly, this self-organizing mechanism is linked to Myosin IIa activity, leading to local pulses of contractile flow. We hypothesize that these pulses of contractile flow are coupled to the extracellular space via focal adhesions, providing a potential link between the underlying signaling network and extracellular matrix elasticity (Fig. 6 a). More rigid substrates enable the generation of stronger intracellular forces, and these increased forces can stimulate the interaction between Myosin IIa and actin filaments and the assembly dynamics of bipolar myosin filaments (Luo et al., 2012). We therefore hypothesized that intracellular contraction pulses might be stimulated on more rigid substrates.

Indeed, the amplitude and rate of spontaneous Myosin IIa localization pulses were significantly increased when cells were plated on stiffer substrates (300 or 500 kPa) as compared with softer substrates (10 kPa). Similar effects were observed in resting (Fig. 6, b-d; and Video 8) and nocodazole-treated cells (Fig. 6, e-g). This shows that the intracellular excitable signal system that forms the basis of spontaneous contractility pulses is coupled to and influenced by the cells' elastic extracellular environment.

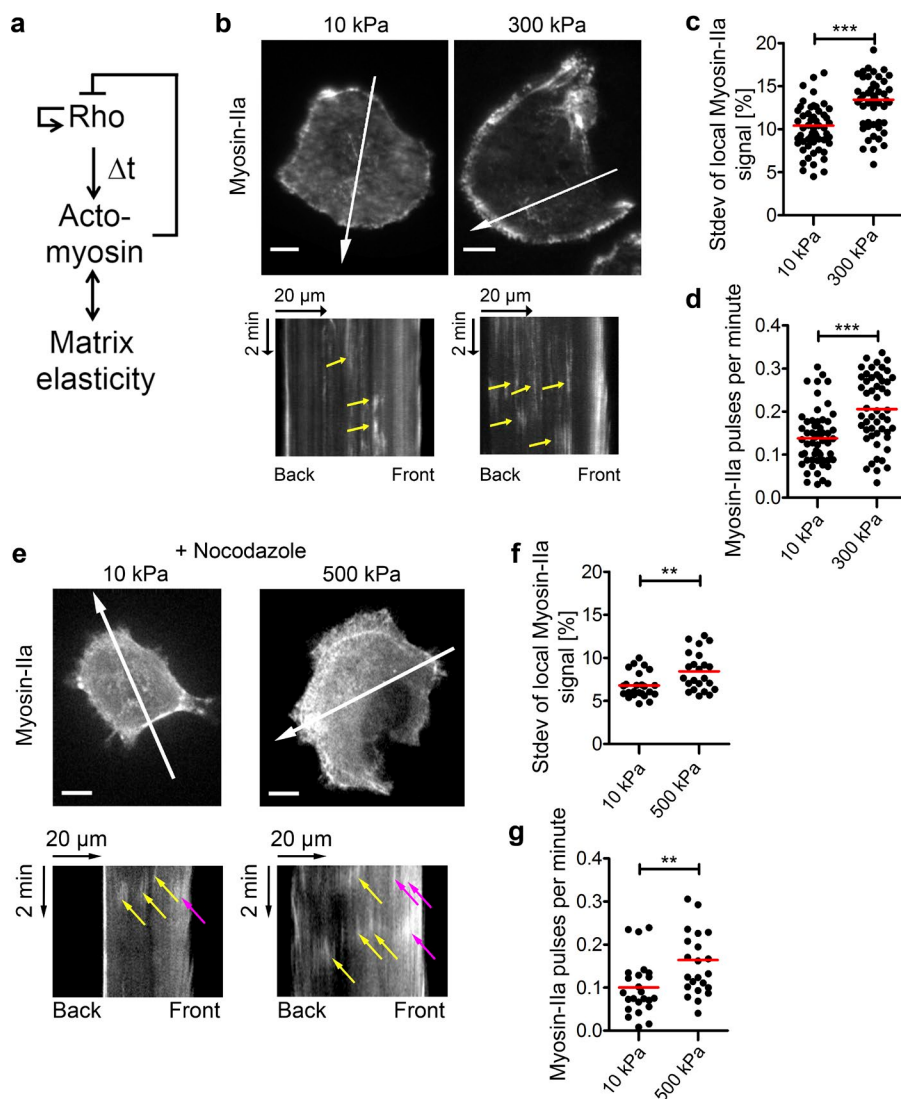


Figure 6. Modulation of Rho activity pulse frequency by matrix elasticity. (a) Schematic of the proposed cross talk between cellular contractility signaling and matrix elasticity. Unreated, resting (b–d) or nocodazole-treated (e–g) U2OS cells were grown on matrices of different elasticities and visualized via TIRFM (b–d) or spinning disk microscopy (e–g; see also Video 8). (b and e) Individual images of Myosin IIa localization; kymographs corresponding to white arrows. Arrows indicate activity pulse peaks at the cell border (magenta) or near the cell center (yellow). (c, d, f, and g) Local standard deviation and frequency of myosin activity pulses (c and d; $n \geq 53$ cells from three experiments) in unstimulated cells or after nocodazole-induced Rho activation (f and g; $n \geq 23$ cells from five experiments). Frame rate is 20/min. Bars, 10 μ m. **, $P < 0.01$; ***, $P < 0.001$ (c, d, f, and g, unpaired t test).

Discussion

Cells adapt their shape to their environment primarily by altering the dynamic organization of their actin cytoskeleton. However, the mechanisms that regulate these dynamic cell-shape changes in space and time are still poorly understood. Here, we show that myosin-based cell contraction is controlled by a signaling network that combines positive and negative feedback on the regulatory small GTPase Rho. Depending on the expression level of the positive feedback mediator GEF-H1, this network manifests distinct dynamic behaviors. In the absence of GEF-H1, the negative feedback is dominant. By itself, a system based on negative feedback displays homeostasis and counteracts the effect of a stimulus (Tyson et al., 2003). Here, this homeostasis can limit the formation of stress fibers. This can be seen in analogy to proprioception in the control of muscle contractility, in which an afferent nerve limits muscle contraction stimulated by an efferent nerve (Johnson et al., 2008). In individual cells, an analogous control system could play a role in balancing protrusive and contractile cell-shape changes.

At endogenous GEF-H1 levels and in the absence of nocodazole, the positive and negative feedbacks are in balance, leading to basal subcellular contractility pulses of varying

amplitude and intermittent, stronger Rho activity pulses. These dynamic activity changes offer a mechanism for cells to continuously probe their environment via associated, dynamic cell contractions and mechanosensitive focal adhesions. Indeed, we found that pulses of this cell contractility network are localized to subcellular areas of the plasma membrane, presumably because of the local accumulation of slowly diffusing, active Rho. Such localized contraction pulses enable local sensing of extracellular cues while preventing global contraction of the entire cell, which could otherwise lead to detachment from its matrix.

Several developmental processes are controlled by the elastic properties of the extracellular environment. For example, differentiation of mesenchymal stem cells to neurons, muscle cells, or bone-forming osteoblasts can be triggered by defined ranges of matrix stiffness and involve Myosin II activity (Engler et al., 2006). Our study reveals a novel, matrix elasticity-modulated signaling network that forms spatiotemporal patterns of protein activity linked to cellular contraction. These spatiotemporal patterns might then be decoded into elasticity-dependent cell differentiation decisions. Local pulses of

contractility were also observed during *Drosophila melanogaster* gastrulation (Martin et al., 2009; Kerridge et al., 2016), suggesting that the excitable Rho/myosin system we describe here might be conserved during evolution. Interestingly, the activity of the GEF-H1-related *Drosophila* protein RhoGEF2 is increased during gastrulation (Martin et al., 2009). It would be interesting to investigate, if this regulator mediates positive feedback of Rho activity in that system.

Increasing Rho self-amplification either by releasing GEF-H1 from microtubules or by overexpression of WT or active GEF-H1 stimulates the formation of propagating contractility waves. The ability to form these waves is presumably a consequence of increased Rho self-amplification, which leads to more robust and thereby self-propagating local Rho activation. Interestingly, wave propagation of cytoskeletal components or their regulators was observed in several distinct contexts (Xiong et al., 2010; Case and Waterman, 2011; Iglesias and Devreotes, 2012; Tang et al., 2014; Bement et al., 2015), suggesting that the underlying network topology of an activator–inhibitor system with excitable properties might be a more general motif to control the spatiotemporal organization of cytoskeletal dynamics. For example, myosin-independent waves of actin polymerization were recently observed during meiosis in the cortex of *Xenopus laevis* and starfish oocytes and embryos (Bement et al., 2015). In that context, the GEF Ect2 was found to be an essential, positive regulator of system dynamics. In contrast, we found that Ect2 is dispensable for spontaneous Rho activity pulses in resting adherent cells and that Ect2 activation induced a distinct wave propagation phenotype in a small subpopulation of cells. Thus, these results show that Ect2 and GEF-H1 trigger distinct wave propagation mechanisms in distinct cellular contexts. Interestingly, seemingly cyclic RhoB activation patterns were observed after nocodazole treatment of primary human endothelial cells (Reinhard et al., 2016). Such patterns were not observed for the related GTPases RhoA and RhoC. It is thus interesting to speculate that human endothelial cells might also use an excitable signaling network to control Rho activity, and it might be interesting to investigate which Rho isoform is relevant for the activity patterns we observe in our study.

In conclusion, we present a Rho/myosin-based activator–inhibitor signaling network that controls localized patterns of cell contractility. This system exhibits irregular or periodic pulses, as well as wave propagation, which enable local sampling at subcellular scales. We propose that this network forms the basis of self-limited, exploratory stress fiber organization and that it is modulated by mechanical and biochemical cues to actively shape individual cells and their arrangement in multicellular structures.

Materials and methods

Cell culture and reagents

Human U2OS osteosarcoma cells (HTB-96; ATCC) were cultured in DMEM-GlutaMAX supplemented with 10% FBS, 50 U/ml penicillin, and 50 µg/ml streptomycin at 37°C and 5% CO₂. In some experiments, cells were treated with 30 µM of the microtubule-depolymerizing compound nocodazole (45–90 min) to stimulate RhoA activity. Pharmacological treatments started 72–78 h after siRNA transfection or 14–20 h after transfection of plasmid DNAs. For live-cell imaging, cells were plated onto collagen type I-coated glass-bottom dishes (1 h, c = 0.01 mg/ml) either before transfection of plasmid DNA or to investigate

cell spreading 0.5–1 h before imaging. To study the effect of matrix elasticity, cells were plated on soft elastomeric substrates made of two different cross-linked silicone rubber systems. For spinning disk microscopy in the presence of nocodazole, Sylgard 184 (Dow Corning GmbH) was used with an elasticity of 500 kPa (20:1 ratio, base to cross-linker WT/WT) and 10 kPa (55:1). For TIRF microscopy in the absence of nocodazole, LS-3252 (NuSil Technology) was used with an elasticity of 10 kPa (1.4:1 ratio, part A to part B WT/WT) and 300 kPa (1:1.6, part A to part B WT/WT) and a refractive index of 1.52. Preparation and characterization of elastomer material properties (Young's modulus and Poisson's ratio) were performed as described previously (Cesa et al., 2007). In brief, prepolymer mixtures were degassed and subsequently spin-coated on ~100-µm-thin coverslips (thickness #0) to obtain an 80-µm-thick elastomer layer. Cross-linking was performed at 60°C overnight. Elastomeric substrates were subsequently glued to the bottom of 3.5-cm Petri dishes to cover predrilled 1.5-cm holes. The BAC-transgenic FHOD1 embryonic stem cell line was generated essentially as described previously (Poser et al., 2008). Embryonic stem cells (cell line R1/E, obtained from A. Bird, Max Planck Institute of Molecular Physiology, Dortmund, Germany) were cultivated on 0.1% gelatin in DMEM with 10% FBS, 50 U/ml penicillin and 50 µg/ml streptomycin, 1% MEM-NEAA, 1% GlutaMAX, 0.1 mM β-Mercaptoethanol and 10 ng/ml leukemia inhibitory factor (LIF; protein factory) at 37°C and 5% CO₂. EGFP and G418 resistance was introduced into the N-terminal region of the FHOD1 gene in BAC RP24-131O24 (Chori) via recombineering. The modified BAC was transfected into embryonic stem cells using Lipofectamine 2000 (Life Technologies), and individual clones were isolated after selection using 200 µg/ml G418. For TIRF microscopy, embryonic stem cells were plated on 5 µg/ml laminin LN511 in the continued presence of LIF.

Constructs and siRNAs

delCMV-mCherry-actin was described previously (Watanabe and Mitchison, 2002; Schulze et al., 2014). The Rho and Cdc42 activity sensors delCMV-EGFP-Rhotekin-GBD, delCMV-mCherry-Rhotekin-GBD and delCMV-WASP-GBD were generated analogously by PCR amplification of the Rhotekin RhoA-binding domain from mCherry-Rhotekin (8–89)-mCherry-C1 (Murakoshi et al., 2011; plasmid 29675; Addgene) and the N-WASP GBD from pΔSV40-mCherry-WASP-GBD (pAL198, plasmid 22281; Addgene; Levskaya et al., 2009) and ligated into delCMV-mCherry/delCMV-EGFP using EcoRI and BamHI sites. The Rac1 activity sensor delCMV-mCherry-p67^{phox}-GBD was generated likewise using pGEX-4T-I-p67^{phox}-aa1–203 (Lapouge et al., 2000; gift of M.R. Ahmadian, Heinrich Heine University, Düsseldorf, Germany) as a PCR template. EGFP-GEF-H1 WT, EGFP-GEF-H1 C53R (deficient in microtubule binding), and EGFP-GEF-H1 C53R Y393A (deficient in microtubule binding and GEF activity) constructs, as well as the siRNA-resistant constructs EGFP-GEF-H1 WT R9 and EGFP-GEF-H1 Y393A R9, were described previously (Krendel et al., 2002; Birkenfeld et al., 2007; Chang et al., 2008). The siRNA-resistant construct EGFP-GEF-H1 WT F539A I541E (deficient in binding to active Rho) was created based on Medina et al. (2013) via site-directed mutagenesis PCR of EGFP-GEF-H1 WT R9 using the primers 5'-CCAGGAGAAAGGGATGGCACTGGAAAGCGCA GCCCACCTGAG-3' and 5'-GGTGGGGCTGCGCTTCCAGT GCCATCCCTTCTCCTGGTTGG-3'. The same primers were used to generate EGFP-GEF-H1 C53R F539A I541E (deficient in binding to microtubules and active Rho) from EGFP-GEF-H1 C53R. EGFP-Ect2 WT and EGFP-Ect2 414–882 (ΔN5; constitutive active as described in Saito et al., 2004) were a gift of J. Birkenfeld (Sanofi Aventis Deutschland GmbH, Frankfurt, Germany). EGFP-NMHCIIA (Wei and Adelstein, 2000; plasmid 11347), GFP-RhoA (Roberts et al.,

2008; plasmid 23224), and mCherry-NMHCIIA (Dulyaninova et al., 2007; plasmid 35687) plasmids were obtained from Addgene. delC-MV-EGFP-FHOD1 WT was described previously (Schönichen et al., 2013). WT p190RhoGAP and its GAP-inactive mutant, p190RhoGAP DN, cloned in pEGFP-C1 were provided by K. Burridge (University of North Carolina, Chapel Hill, NC; Maddox and Burridge, 2003). pEGFP-Myo9b and its GAP-inactive mutant, pEGFP-Myo9b-R1695M, were supplied by M. Bähler (University of Münster, Münster, Germany; van den Boom et al., 2007). EGFP-CAAX was a gift of P. Bastiaens (Max Planck Institute of Molecular Physiology, Dortmund, Germany). GFP-LARG FL was provided by P.B. Wedegaertner (Thomas Jefferson University, Philadelphia, PA; Grabocka and Wedegaertner, 2007). All plasmid DNA was transfected using Lipofectamine 2000. siRNAs were purchased from GE Healthcare Dharmacon. ON-TARGETplus siRNA GEF-H1 #9 (LQ-009883-00-0002) was used to deplete GEF-H1 (Chang et al., 2008). ON-TARGETplus SMARTpool Ect2 siRNA was used to deplete Ect2 (L-006450-00-0005). ON-TARGETplus nontargeting siRNA #2 (D-0018-10-02-05) was used as control (ntsiRNA). U2OS cells were transfected with 5 nM of the respective siRNAs immediately after plating (fast forward transfection) using HiPerFect (Qiagen) and replated on the next day. Subsequent experiments were performed 72 h after siRNA transfection. Knockdown efficiency was determined by Western blot analysis.

Immunofluorescence

Untreated cells or cells treated with 30 μM nocodazole for 45 or 90 min were fixed with ice-cold methanol for 20 min at -20°C, washed three times with PBS, and incubated in blocking solution (2% BSA in PBS) for 1 h at RT. Coverslips were incubated with anti-α-tubulin antibody (1:500 [MCA77G]; Bio-Rad) in blocking solution for 1 h, washed with PBS, and incubated with Alexa Fluor 488-conjugated goat anti-rat secondary antibody (1:500; Invitrogen) in blocking solution for 1 h at RT. Samples were washed with PBS and mounted on glass slides using ProLong Gold antifade reagent (Invitrogen).

Western blot analysis

Cells were washed once with ice-cold PBS and lysed in ice-cold RIPA buffer (50 mM Tris, pH 7.5, 150 mM NaCl, 1% NP-40, 0.25% sodium deoxycholate, 1 mM EDTA, 1× protease inhibitor cocktail, and 1× phosphatase inhibitor cocktail). Cell debris was removed by centrifugation at 14,000 g for 15 min at 4°C. Protein concentration in the supernatants was determined via Bradford assay. Equal amounts of total protein were mixed with 5× Laemmli sample buffer, boiled at 95°C for 10 min and separated by SDS-PAGE. After electrophoresis, proteins were transferred on a PVDF membrane using a semidry blotter. Blots were blocked for 30–60 min at RT with 5% BSA in TBS-T (20 mM Tris, pH 7.6, 137 mM NaCl, and 0.1% Tween-20) and incubated overnight at 4°C with primary antibodies anti-GEF-H1 (1:200; 55B6; Cell Signaling), anti-Ect2 (1:500; C-20; Santa Cruz Biotechnology), and anti-α-Tubulin (1:20,000; clone B-5-1-2; Sigma-Aldrich) in blocking solution. Membranes were washed three times with TBS-T and incubated with HRP-conjugated anti-mouse (for anti-α-Tubulin) or anti-rabbit (for anti-GEF-H1) secondary antibodies (1:20,000) for 1 h at RT. After additional washing steps with TBS-T and TBS (20 mM Tris, pH 7.6, and 137 mM NaCl), proteins were visualized with ECL Western blotting substrate.

Microscopy

TIRF and confocal spinning disk microscopy were performed on an Eclipse Ti-E (Nikon) inverted microscope with a motorized TIRF Illuminator Unit, an AOTF Laser Combiner, a laser dual spinning disk scan head (CSU-X1; Yokogawa), and an iXon3 897 single-photon-detection EMCCD camera. Laser lines used for excitation of EGFP and mCherry

were 488 and 561 nm, respectively. Images were acquired using an Apo TIRF 100× 1.49 NA oil-immersion objective (Nikon) with an EM gain of 50–100 and 2 × 2 binning. A dual bandpass dichroic mirror (zt488/561rpc) was used in combination with a CSU Quad Dichroic mirror/emission filter set (405/488/568/647 nm). Acquisition was controlled by Andor IQ Software. In some experiments, TIRF microscopy was conducted on an IX-81 microscope (Olympus), equipped with a TIRF-MITICO motorized TIRF illumination combiner, an Apo TIRF 60× 1.45 NA oil-immersion objective and a ZDC autofocus device. On that setup, a triple bandpass dichroic mirror (U-M3TIR405/488/561,) was used in combination with an emission filter set (HC 520/35 and HC 629/53), the 488 nm line of a 400-mW argon ion laser, and the Cell R diode laser 561 (100 mW). For detection, this was combined with an EMCCD camera at medium gain without binning. Both microscopes are equipped with temperature-controlled incubation chambers. Time-lapse live-cell microscopy experiments were performed at 37°C in CO₂-independent medium (HBSS buffer, 10% FBS, 2 mM L-Glutamine, 10 mM Hepes, 1 mM MgCl₂, and 1 mM CaCl₂) with indicated frame rates. Confocal laser scanning microscopy of fixed cells was performed on a TCS SP5 AOBS system (Leica Microsystems) equipped with an HCX PL APO 63×/1.4 NA oil-immersion objective. Excitation of Alexa Fluor 488 was performed with the 488-nm line of an argon laser. Fluorescence was measured using the HyD detector (490–540 nm). Acquisition was controlled using LASAF software (Leica Microsystems). Confocal z stacks were acquired with 210-nm spacing, and maximum projections were generated with ImageJ.

Characterization of the mCherry-p67phox-GBD-based Rac1 activity sensor by optogenetics

HeLa cells cultured using standard conditions were cotransfected on fibronectin-coated (Sigma Aldrich) LabTek plates with the Rac1 activity sensor construct (mCherry-p67phox-GBD) and photoactivatable Rac1 (mCitrine-PA-Rac1; Wu et al., 2009) using XtremeGene 9 (Roche Diagnostics). Light-based activation of mCitrine-PA-Rac1 was performed by wide-field illumination using a Brightline HC 427/10 filter (Semrock) in the MT-20 illumination device (Olympus). The built-in neutral-density filter wheel of the MT-20 device was used to control light intensity. To prevent saturated PA-Rac1 activation at low intensity settings, an additional 1,000× neutral-density filter was added into the blue light-illumination light path. Rac1 activity sensor signal measurements were performed using TIRF illumination at 561 nm essentially as described in the previous paragraph (TIRF-M system; Olympus).

Data analysis

Except if noted otherwise, we considered the entire adhesion area of the cell for quantitative analysis of signal changes and cross-correlation. Therefore, measurements of peak width, frequency, height, and cross-correlation were averaged over the whole cell and were usually lower than measurements shown in selected cell areas.

Spatial and temporal cross-correlation analyses. To determine the temporal cross-correlation functions, image sequences were obtained at a frame rate of 20/min. To minimize influence of noise, images were obtained with 2 × 2 binning and in addition, image x-y resolution was scaled down by a factor of 15–20 using the averaging command in ImageJ. The Pearson product-moment correlation coefficient of time-shifted corresponding images was calculated using custom Matlab scripts. To determine the spatiotemporal cross-correlation function, the original 2 × 2-binned image sequences were used, in which time shifting was combined with spatial shifting of corresponding image sequences by steps of four pixels. Half-time and decay length of cross-correlation analyses were obtained by fitting the corresponding graphs to monoexponential decay functions.

Radial intensity distribution. Analysis of the radial intensity distribution was performed similarly as described previously (Möhl et al., 2012). In brief, all 150 frames of image sequences from spreading cells were included in the analysis. The centroid of cells was determined in each frame via the built-in ImageJ function and used for polar coordinate transformation by an external ImageJ plugin (<http://rsb.info.nih.gov/ij/plugins/polar-transformer.html>). Polar transformed images were stretched to reach a constant radius via linear interpolation. The mean distribution corresponding to all angles and frames from the centroid to the periphery was calculated via a custom-built ImageJ macro.

Analysis of standard deviation, mean frequency, peak amplitude, and peak width of activity pulses. Because of the irregular nature of the majority of activity pulses, standard methods to study more regular oscillations, such as Fourier analysis, were not optimal. Instead, we analyzed the variation of signal intensity in time series to directly extract their characteristics using a custom-built ImageJ macro. In brief, image sequences were obtained at a frame rate of 3 or 20 per minute with 2×2 binning and scaled down by a factor of 15–20 using averaging to reduce noise. Individual cells in image sequences were isolated, masked, and corrected for background intensity. The peripheral pixels were removed using a single application of the binary erode filter with neighborhood count of 1 to avoid measurements of signal changes that originate from dynamic cell protrusion and to focus analysis of the analysis of signal dynamics in the cell center. Global intensity changes that affect the entire cell were removed by normalizing signals to the mean background-corrected intensity in each time frame. In each pixel, intensity changes were determined over time and analyzed as follows. To directly obtain the overall local variability associated with irregular activity pulses, the standard deviation was calculated for each scaled-down pixel over time. We called this normalized measurement “local standard deviation.” To identify intensity peaks, the intensity was analyzed in each pixel at each time point of the time series. Only, if the intensity at the given time point was higher than the following and preceding intensity, a time point was considered a peak. To limit the effect of noise, only those peaks that were >1% of the mean intensity of the time series were measured. In addition, a walking mean of seven frames was calculated for videos with a frame rate of 20 per minute. The peak height was determined as the difference between the peak intensity and the mean of the following and preceding intensity minima. The peak width was determined as the time difference between these intensity minima. To analyze pulse frequency, only the most prominent peaks that were >10% of the mean intensity of the time-series were counted. Generation of graphs, curve fitting and statistical analysis were performed using GraphPad Prism 5 software. Red lines in scatter dot plots denote mean values. Stars denote p-values for indicated statistical tests (*, P < 0.05; **, P < 0.01; ***, P < 0.001). Figures were prepared using Photoshop CS2014 (Adobe).

STICS analysis. STICS analysis was used to generate vector maps of the flow of myosin signal inhomogeneities. Analysis was performed on myosin image sequences (20 frames/min) using an ImageJ plugin (http://research.stowers.org/imagejplugins/ics_plugins.html). A custom ImageJ macro was used to calculate a series of vector maps, each of which was based on subsequences containing two frames before and after the respective time point. The divergence of each vector map was determined using the built-in Matlab function. The inward flow of the vector map corresponds to the negation of the divergence and thus represents the contractile flow of the myosin signal inhomogeneities.

Fourier analysis. To analyze the regular oscillations that were induced by overexpression of Myo9b, we generated the power spectrum of intensity time series via a fast-Fourier transform algorithm. First, the image x-y resolution of time series was scaled down by a factor of 15

using averaging, and the resulting time series were analyzed separately in each pixel. The time series were divided by the mean intensity, and a constant value of 1 was subtracted to normalize the mean intensity to 0. The decrease in the intensity baseline caused by bleaching was obtained by fitting the mean signal from individual cells to the “one-phase decay” function using Prism, followed by baseline subtraction. Fourier transformation was performed by sequential application of the “stack temporal fft jeu v1” and the “complex amp jeu v1” ImageJ plugins (http://research.stowers.org/imagejplugins/ics_plugins.html). The mean power spectrum per cell was obtained from the plugin output via the “Plot Z-axis Profile” ImageJ function.

Online supplemental material

Fig. S1 shows Rho activity, myosin localization dynamics, and control measurements in resting and spreading cells. Fig. S2 shows nocodazole-treatment control experiments, Rho activity dynamics, and control measurements in resting, nocodazole-treated, GEF-H1-depleted and LARG-overexpressing cells and Western blots of siRNA-treated cells. Fig. S3 shows RhoA localization dynamics, Rac1 sensor control experiments, and cross-correlation analyses of Rho activity with Rac1 or Cdc42 activity or FHOD1 localization and FHOD1 localization dynamics in embryonic stem cells. Fig. S4 shows a scheme for contractile node formation and cross-correlation analyses of Rho activity with WT or GAP-deficient p190RhoGAP. Fig. S5 shows Rho activity dynamics before and after Y27632 treatment and control experiments for blebbistatin and Y27632. Video 1 shows Rho activity dynamics in resting and nocodazole-treated cells. Video 2 shows Rho activity dynamics in GEF-H1 C53R-overexpressing cells. Video 3 shows Rho activity dynamics in GEF-H1-overexpressing and GEF-H1-depleted cells. Video 4 shows analyses of Rho activity together with control sensor (EGFP only), GEF-H1 localization, Cdc42 activity, and Rac1 activity. Video 5 shows analyses of Rho activity together with myosin localization. Video 6 shows Rho activity dynamics in the presence of WT or GAP-deficient Myo9b. Video 7 shows Rho activity and myosin localization before and after blebbistatin treatment. Video 8 shows myosin localization dynamics on elastic surfaces.

Acknowledgments

We thank Sven Müller (Max Planck Institute of Molecular Physiology [MPI Dortmund]) for expert microscopy support, Reza Ahmadian for helping in the design and generation of the Rac1 activity sensor, and Alex Bird and Arnaud Rondelet (MPI Dortmund) for advice and guidance in the generation of the BAC-transgenic embryonic stem cell line. We also thank Oliver Rocks (Max Delbrück Center for Molecular Medicine), Malte Schmick (MPI Dortmund), and Aneta Koseska (MPI Dortmund) for helpful discussions and Philippe Bastiaens (MPI Dortmund) for departmental support and helpful discussions.

This work was supported by Mercator Research Center Ruhr (MERCUR grant Pr-2012-0022 to P. Nalbant and L. Dehmelt), the Forschungseinheiten der Systembiologie (FORSYS) partner initiative (Bundesministerium für Bildung und Forschung grant 0315258 to L. Dehmelt), Deutsche Forschungsgemeinschaft Priority Program SPP 1462/2 (to P. Nalbant), the Marie Skłodowska-Curie Innovative Training Network InCeM (European Union, Call H2020-MSCA-ITN-2014; project ID 642866 to P. Nalbant and L. Dehmelt), and the Deutsche Forschungsgemeinschaft Heisenberg Program (L. Dehmelt).

The authors declare no competing financial interests.

Author contributions: P. Nalbant and L. Dehmelt conceived the research concept, supervised experiments and wrote the manuscript. M. Graessl and J. Koch performed the majority of experiments and

analyses and contributed to manuscript preparation. A. Calderon generated and characterized Rho, Cdc42, and Rac1 activity sensors. D. Solouk contributed to Rac1 activity sensor development and characterization. L. Dehmelt, S. Banerjee, and T. Mazel developed image and data analysis methods. D. Kamps performed and analyzed experiments using the amplification-deficient GEF-H1 triple mutant C53R F539A I541E. N. Schulze performed western blot analyses and contributed to microscopy optimization. J.K. Jungkurth generated and analyzed the stable FHOD1-expressing embryonic stem cell line. R. Patwardhan performed and analyzed control experiments using EGFP-CAAX. N. Hampe generated the elastomeric substrates. B. Hoffmann supervised the preparation of elastomeric substrates.

Submitted: 10 June 2017

Revised: 25 August 2017

Accepted: 8 September 2017

References

- Arthur, W.T., and K. Burridge. 2001. RhoA inactivation by p190RhoGAP regulates cell spreading and migration by promoting membrane protrusion and polarity. *Mol. Biol. Cell.* 12:2711–2720. <https://doi.org/10.1091/mbc.12.9.2711>
- Barnhart, E.L., J. Allard, S.S. Lou, J.A. Theriot, and A. Mogilner. 2017. Adhesion-Dependent Wave Generation in Crawling Cells. *Curr. Biol.* 27:27–38. <https://doi.org/10.1016/j.cub.2016.11.011>
- Bement, W.M., M. Leda, A.M. Moe, A.M. Kita, M.E. Larson, A.E. Golding, C. Pfeuti, K.C. Su, A.L. Miller, A.B. Goryachev, and G. von Dassow. 2015. Activator-inhibitor coupling between Rho signalling and actin assembly makes the cell cortex an excitable medium. *Nat. Cell Biol.* 17:1471–1483. <https://doi.org/10.1038/ncb3251>
- Benink, H.A., and W.M. Bement. 2005. Concentric zones of active RhoA and Cdc42 around single cell wounds. *J. Cell Biol.* 168:429–439. <https://doi.org/10.1083/jcb.200411109>
- Birkenfeld, J., P. Nalbant, B.P. Bohl, O. Pertz, K.M. Hahn, and G.M. Bokoch. 2007. GEF-H1 modulates localized RhoA activation during cytokinesis under the control of mitotic kinases. *Dev. Cell.* 12:699–712. <https://doi.org/10.1016/j.devcel.2007.03.014>
- Burnette, D.T., S. Manley, P. Sengupta, R. Sougrat, M.W. Davidson, B. Kachar, and J. Lippincott-Schwartz. 2011. A role for actin arcs in the leading-edge advance of migrating cells. *Nat. Cell Biol.* 13:371–381. <https://doi.org/10.1038/ncb2205>
- Case, L.B., and C.M. Waterman. 2011. Adhesive F-actin waves: a novel integrin-mediated adhesion complex coupled to ventral actin polymerization. *PLoS One.* 6:e26631. <https://doi.org/10.1371/journal.pone.0026631>
- Cesa, C.M., N. Kirchgessner, D. Mayer, U.S. Schwarz, B. Hoffmann, and R. Merkel. 2007. Micropatterned silicone elastomer substrates for high resolution analysis of cellular force patterns. *Rev. Sci. Instrum.* 78:034301. <https://doi.org/10.1063/1.2712870>
- Chang, C.W., and S. Kumar. 2015. Differential Contributions of Nonmuscle Myosin II Isoforms and Functional Domains to Stress Fiber Mechanics. *Sci. Rep.* 5:13736. <https://doi.org/10.1038/srep13736>
- Chang, Y.C., P. Nalbant, J. Birkenfeld, Z.F. Chang, and G.M. Bokoch. 2008. GEF-H1 couples nocodazole-induced microtubule disassembly to cell contractility via RhoA. *Mol. Biol. Cell.* 19:2147–2153. <https://doi.org/10.1091/mbc.E07-12-1269>
- Chen, Z., F. Medina, M.Y. Liu, C. Thomas, S.R. Sprang, and P.C. Sternweis. 2010. Activated RhoA binds to the pleckstrin homology (PH) domain of PDZ-RhoGEF, a potential site for autoregulation. *J. Biol. Chem.* 285:21070–21081. <https://doi.org/10.1074/jbc.M110.122549>
- Dulyaninova, N.G., R.P. House, V. Betapudi, and A.R. Bresnick. 2007. Myosin-IIA heavy-chain phosphorylation regulates the motility of MDA-MB-231 carcinoma cells. *Mol. Biol. Cell.* 18:3144–3155. <https://doi.org/10.1091/mbc.E06-11-1056>
- Engler, A.J., S. Sen, H.L. Sweeney, and D.E. Discher. 2006. Matrix elasticity directs stem cell lineage specification. *Cell.* 126:677–689. <https://doi.org/10.1016/j.cell.2006.06.044>
- Fitzhugh, R. 1961. Impulses and Physiological States in Theoretical Models of Nerve Membrane. *Biophys. J.* 1:445–466. [https://doi.org/10.1016/S0006-3495\(61\)86902-6](https://doi.org/10.1016/S0006-3495(61)86902-6)
- Frick, M., K. Schmidt, and B.J. Nichols. 2007. Modulation of lateral diffusion in the plasma membrane by protein density. *Curr. Biol.* 17:462–467. <https://doi.org/10.1016/j.cub.2007.01.069>
- Grabocka, E., and P.B. Wedegaertner. 2007. Disruption of oligomerization induces nucleocytoplasmic shuttling of leukemia-associated rho Guanine-nucleotide exchange factor. *Mol. Pharmacol.* 72:993–1002. <https://doi.org/10.1124/mol.107.035162>
- Grecco, H.E., M. Schmick, and P.I. Bastiaens. 2011. Signaling from the living plasma membrane. *Cell.* 144:897–909. <https://doi.org/10.1016/j.cell.2011.01.029>
- Guilluy, C., R. Garcia-Mata, and K. Burridge. 2011. Rho protein crosstalk: another social network? *Trends Cell Biol.* 21:718–726. <https://doi.org/10.1016/j.tcb.2011.08.002>
- Iglesias, P.A., and P.N. Devreotes. 2012. Biased excitable networks: how cells direct motion in response to gradients. *Curr. Opin. Cell Biol.* 24:245–253. <https://doi.org/10.1016/j.ceb.2011.11.009>
- Johnson, E.O., G.C. Babis, K.C. Soulantasis, and P.N. Soucacos. 2008. Functional neuroanatomy of proprioception. *J. Surg. Orthop. Adv.* 17:159–164.
- Kerridge, S., A. Munjal, J.M. Philippe, A. Jha, A.G. de las Bayonas, A.J. Saurin, and T. Lecuit. 2016. Modular activation of Rho1 by GPCR signalling imparts polarized myosin II activation during morphogenesis. *Nat. Cell Biol.* 18:261–270. <https://doi.org/10.1038/ncb3302>
- Krendel, M., F.T. Zenke, and G.M. Bokoch. 2002. Nucleotide exchange factor GEF-H1 mediates cross-talk between microtubules and the actin cytoskeleton. *Nat. Cell Biol.* 4:294–301. <https://doi.org/10.1038/ncb773>
- Kühn, S., and M. Geyer. 2014. Formins as effector proteins of Rho GTPases. *Small GTPases.* 5:e29513. <https://doi.org/10.4161/sgrp.29513>
- Lapouge, K., S.J. Smith, P.A. Walker, S.J. Gamblin, S.J. Smerdon, and K. Rittinger. 2000. Structure of the TPR domain of p67phox in complex with Rac.GTP. *Mol. Cell.* 6:899–907. [https://doi.org/10.1016/S1097-2765\(00\)901-2](https://doi.org/10.1016/S1097-2765(00)901-2)
- Lee, C.S., C.K. Choi, E.Y. Shin, M.A. Schwartz, and E.G. Kim. 2010. Myosin II directly binds and inhibits Dbl family guanine nucleotide exchange factors: A possible link to Rho family GTPases. *J. Cell Biol.* 190:663–674. <https://doi.org/10.1083/jcb.201003057>
- Levkaya, A., O.D. Weiner, W.A. Lim, and C.A. Voigt. 2009. Spatiotemporal control of cell signalling using a light-switchable protein interaction. *Nature.* 461:997–1001. <https://doi.org/10.1038/nature08446>
- Luo, T., K. Mohan, V. Srivastava, Y. Ren, P.A. Iglesias, and D.N. Robinson. 2012. Understanding the cooperative interaction between myosin II and actin cross-linkers mediated by actin filaments during mechanosensation. *Biophys. J.* 102:238–247. <https://doi.org/10.1016/j.bpj.2011.12.020>
- Machacek, M., L. Hodgson, C. Welch, H. Elliott, O. Pertz, P. Nalbant, A. Abell, G.L. Johnson, K.M. Hahn, and G. Danuser. 2009. Coordination of Rho GTPase activities during cell protrusion. *Nature.* 461:99–103. <https://doi.org/10.1038/nature08242>
- Maddox, A.S., and K. Burridge. 2003. RhoA is required for cortical retraction and rigidity during mitotic cell rounding. *J. Cell Biol.* 160:255–265. <https://doi.org/10.1083/jcb.200207130>
- Martin, A.C., M. Kaschube, and E.F. Wieschaus. 2009. Pulsed contractions of an actin-myosin network drive apical constriction. *Nature.* 457:495–499. <https://doi.org/10.1038/nature07522>
- Medina, F., A.M. Carter, O. Dada, S. Gutowski, J. Hadas, Z. Chen, and P.C. Sternweis. 2013. Activated RhoA is a positive feedback regulator of the Lbc family of Rho guanine nucleotide exchange factor proteins. *J. Biol. Chem.* 288:11325–11333. <https://doi.org/10.1074/jbc.M113.450056>
- Miao, Y., S. Bhattacharya, M. Edwards, H. Cai, T. Inoue, P.A. Iglesias, and P.N. Devreotes. 2017. Altering the threshold of an excitable signal transduction network changes cell migratory modes. *Nat. Cell Biol.* 19:329–340. <https://doi.org/10.1038/ncb3495>
- Möhl, C., N. Kirchgessner, C. Schäfer, B. Hoffmann, and R. Merkel. 2012. Quantitative mapping of averaged focal adhesion dynamics in migrating cells by shape normalization. *J. Cell Sci.* 125:155–165. <https://doi.org/10.1242/jcs.090746>
- Müller, R.T., U. Honnert, J. Reinhard, and M. Bähler. 1997. The rat myosin myr 5 is a GTPase-activating protein for Rho in vivo: essential role of arginine 1695. *Mol. Biol. Cell.* 8:2039–2053. <https://doi.org/10.1091/mbc.8.10.2039>
- Murakoshi, H., H. Wang, and R. Yasuda. 2011. Local, persistent activation of Rho GTPases during plasticity of single dendritic spines. *Nature.* 472:100–104. <https://doi.org/10.1038/nature09823>
- Murray, J.D. 2002. Mathematical Biology: I: An Introduction. Springer, New York. 551 pp.

- Nagumo, J., S. Animoto, and S. Yoshizawa. 1962. An active pulse transmission line simulating nerve axon. *Proc. Inst. Radio Eng.* 50:2061–2070.
- Nishikawa, M., S.R. Naganathan, F. Julicher, and S.W. Grill. 2017. Controlling contractile instabilities in the actomyosin cortex. *eLife*. 6: e19595.
- Poser, I., M. Sarov, J.R. Hutchins, J.K. Hériché, Y. Toyoda, A. Pozniakovsky, D. Weigl, A. Nitzsche, B. Hegemann, A.W. Bird, et al. 2008. BAC TransgeneOmics: a high-throughput method for exploration of protein function in mammals. *Nat. Methods*. 5:409–415. <https://doi.org/10.1038/nmeth.1199>
- Reid, T., T. Furuyashiki, T. Ishizaki, G. Watanabe, N. Watanabe, K. Fujisawa, N. Morii, P. Madaule, and S. Narumiya. 1996. Rhotekin, a new putative target for Rho bearing homology to a serine/threonine kinase, PKN, and rhophilin in the rho-binding domain. *J. Biol. Chem.* 271:13556–13560. <https://doi.org/10.1074/jbc.271.23.13556>
- Reinhard, N.R., S.F. van Helden, E.C. Anthony, T. Yin, Y.I. Wu, J. Goedhart, T.W. Gadella, and P.L. Hordijk. 2016. Spatiotemporal analysis of RhoA/B/C activation in primary human endothelial cells. *Sci. Rep.* 6:25502. <https://doi.org/10.1038/srep25502>
- Ren, X.D., W.B. Kiosses, and M.A. Schwartz. 1999. Regulation of the small GTP-binding protein Rho by cell adhesion and the cytoskeleton. *EMBO J.* 18:578–585. <https://doi.org/10.1093/emboj/18.3.578>
- Riento, K., and A.J. Ridley. 2003. Rocks: multifunctional kinases in cell behaviour. *Nat. Rev. Mol. Cell Biol.* 4:446–456. <https://doi.org/10.1038/nrm1128>
- Roberts, P.J., N. Mitin, P.J. Keller, E.J. Chenette, J.P. Madigan, R.O. Currin, A.D. Cox, O. Wilson, P. Kirschmeier, and C.J. Der. 2008. Rho Family GTPase modification and dependence on CAAX motif-signalated posttranslational modification. *J. Biol. Chem.* 283:25150–25163. <https://doi.org/10.1074/jbc.M800882200>
- Saito, X.-F. Liu, K. Kamijo, R. Raziuddin, T. Tatsumoto, I. Okamoto, X. Chen, C.-C. Lee, M.V. Lorenzi, N. Ohara, and T. Miki. 2004. Dereulation and Mislocalization of the Cytokinesis Regulator ECT2 Activate the Rho Signaling Pathways Leading to Malignant Transformation. *J. Cell Biol.* 279:7169–7179. <https://doi.org/10.1074/jbc.M306725200>
- Schönichen, A., H.G. Mannherz, E. Behrmann, A.J. Mazur, S. Kühn, U. Silván, C.A. Schoenenberger, O.T. Fackler, S. Raunser, L. Dehmelt, and M. Geyer. 2013. FHOD1 is a combined actin filament capping and bundling factor that selectively associates with actin arcs and stress fibers. *J. Cell Sci.* 126:1891–1901. <https://doi.org/10.1242/jcs.126706>
- Schulze, N., M. Graessl, A. Blancke Soares, M. Geyer, L. Dehmelt, and P. Nalbant. 2014. FHOD1 regulates stress fiber organization by controlling the dynamics of transverse arcs and dorsal fibers. *J. Cell Sci.* 127:1379–1393. <https://doi.org/10.1242/jcs.134627>
- Stricker, J., S. Cookson, M.R. Bennett, W.H. Mather, L.S. Tsimring, and J. Hasty. 2008. A fast, robust and tunable synthetic gene oscillator. *Nature*. 456:516–519. <https://doi.org/10.1038/nature07389>
- Symons, M., J.M. Derry, B. Karlak, S. Jiang, V. Lemahieu, F. McCormick, U. Francke, and A. Abo. 1996. Wiskott-Aldrich syndrome protein, a novel effector for the GTPase CDC42Hs, is implicated in actin polymerization. *Cell*. 84:723–734. [https://doi.org/10.1016/S0092-8674\(00\)81050-8](https://doi.org/10.1016/S0092-8674(00)81050-8)
- Takeya, R., K. Taniguchi, S. Narumiya, and H. Sumimoto. 2008. The mammalian formin FHOD1 is activated through phosphorylation by ROCK and mediates thrombin-induced stress fibre formation in endothelial cells. *EMBO J.* 27:618–628. <https://doi.org/10.1038/emboj.2008.7>
- Tang, M., M. Wang, C. Shi, P.A. Iglesias, P.N. Devreotes, and C.H. Huang. 2014. Evolutionarily conserved coupling of adaptive and excitable networks mediates eukaryotic chemotaxis. *Nat. Commun.* 5:5175. <https://doi.org/10.1038/ncomms5175>
- Tyson, J.J., K.C. Chen, and B. Novak. 2003. Sniffers, buzzers, toggles and blinkers: dynamics of regulatory and signaling pathways in the cell. *Curr. Opin. Cell Biol.* 15:221–231. [https://doi.org/10.1016/S0955-0674\(03\)00017-6](https://doi.org/10.1016/S0955-0674(03)00017-6)
- van den Boom, F., H. Düssmann, K. Uhlenbrock, M. Abouhamad, and M. Bähler. 2007. The Myosin IXB motor activity targets the myosin IXB RhoGAP domain as cargo to sites of actin polymerization. *Mol. Biol. Cell*. 18:1507–1518. <https://doi.org/10.1091/mbc.E06-08-0771>
- van Haastert, P.J., I. Keizer-Gunnink, and A. Kortholt. 2017. Coupled excitable Ras and F-actin activation mediates spontaneous pseudopod formation and directed cell movement. *Mol. Biol. Cell*. 28:922–934. <https://doi.org/10.1091/mbc.E16-10-0733>
- Vicente-Manzanares, M., X. Ma, R.S. Adelstein, and A.R. Horwitz. 2009. Non-muscle myosin II takes centre stage in cell adhesion and migration. *Nat. Rev. Mol. Cell Biol.* 10:778–790. <https://doi.org/10.1038/nrm2786>
- Watanabe, N., and T.J. Mitchison. 2002. Single-molecule speckle analysis of actin filament turnover in lamellipodia. *Science*. 295:1083–1086. <https://doi.org/10.1126/science.1067470>
- Wei, Q., and R.S. Adelstein. 2000. Conditional expression of a truncated fragment of nonmuscle myosin II-A alters cell shape but not cytokinesis in HeLa cells. *Mol. Biol. Cell*. 11:3617–3627. <https://doi.org/10.1091/mbc.11.10.3617>
- Winfree, A.T. 1984. The prehistory of the Belousov-Zhabotinsky oscillator. *J. Chem. Educ.* 61:661. <https://doi.org/10.1021/ed061p661>
- Wu, M., X. Wu, and P. De Camilli. 2013. Calcium oscillations-coupled conversion of actin travelling waves to standing oscillations. *Proc. Natl. Acad. Sci. USA*. 110:1339–1344. <https://doi.org/10.1073/pnas.1221538110>
- Wu, Y.I., D. Frey, O.I. Lungu, A. Jaehrig, I. Schlichting, B. Kuhlman, and K.M. Hahn. 2009. A genetically encoded photoactivatable Rac controls the motility of living cells. *Nature*. 461:104–108. <https://doi.org/10.1038/nature08241>
- Xiong, Y., C.H. Huang, P.A. Iglesias, and P.N. Devreotes. 2010. Cells navigate with a local-excitation, global-inhibition-biased excitable network. *Proc. Natl. Acad. Sci. USA*. 107:17079–17086. <https://doi.org/10.1073/pnas.1011271107>
- Yang, H.W., S.R. Collins, and T. Meyer. 2016. Locally excitable Cdc42 signals steer cells during chemotaxis. *Nat. Cell Biol.* 18:191–201.

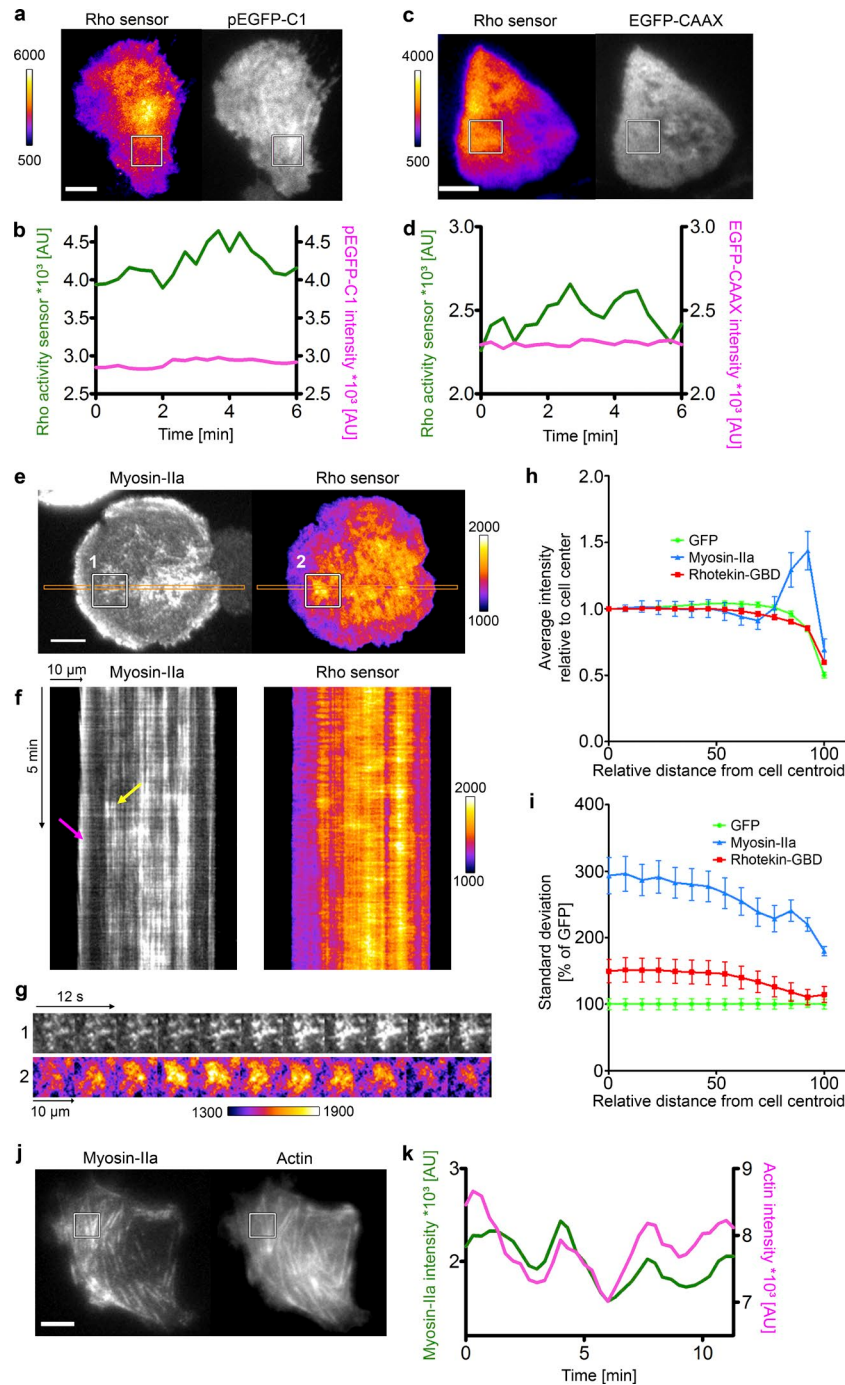
Graessl et al., <https://doi.org/10.1083/jcb.201706052>

Figure S1. Dynamics of Rho activity and Myosin IIa localization in resting cells and during cell spreading. (a–d) Direct comparison of Rho sensor and cytosolic (a and b) or plasma membrane–anchored (c and d) control sensor signals in resting cells. (a and c) Representative TIRF images of cells coexpressing Rho and control sensors. (b and d) Raw profiles of fluorescence signals measured within white boxes in a and c. (e–i) U2OS cells expressing the Rho activity sensor mCherry-Rhotekin-GBD and Myosin IIa (EGFP-NMHCIIa) or EGFP (control) were imaged via time-lapse TIRF microscopy 30–60 min after plating on collagen-coated glass surfaces. (e) Representative TIRF images demonstrating the plasma membrane association of Myosin IIa (EGFP-NMHCIIa) and the Rho activity sensor during cell spreading. (f) Kymographs of regions labeled in e (orange rectangles). (g) Enlarged regions corresponding to white boxes 1 and 2 in panel e. (h and i) Plot of the radial intensity distribution (h) and radial distribution of the standard deviation (i) over time. The standard deviation was first normalized to mean intensity values in individual cells and then normalized to the mean standard deviation value of GFP controls (h and i; $n \geq 24$ cells from three experiments; error bars represent SEM). (j and k) Myosin and actin plasma membrane localization pulses in the absence of the Rho activity sensor. (j) Representative TIRF images of cells coexpressing EGFP-NMHCIIa and mCherry-actin. (k) Intensity measurements within the white box in j. Frame rate is 20/min (e–i) or 3/min (a–d and j–k). Bars, 10 μm.

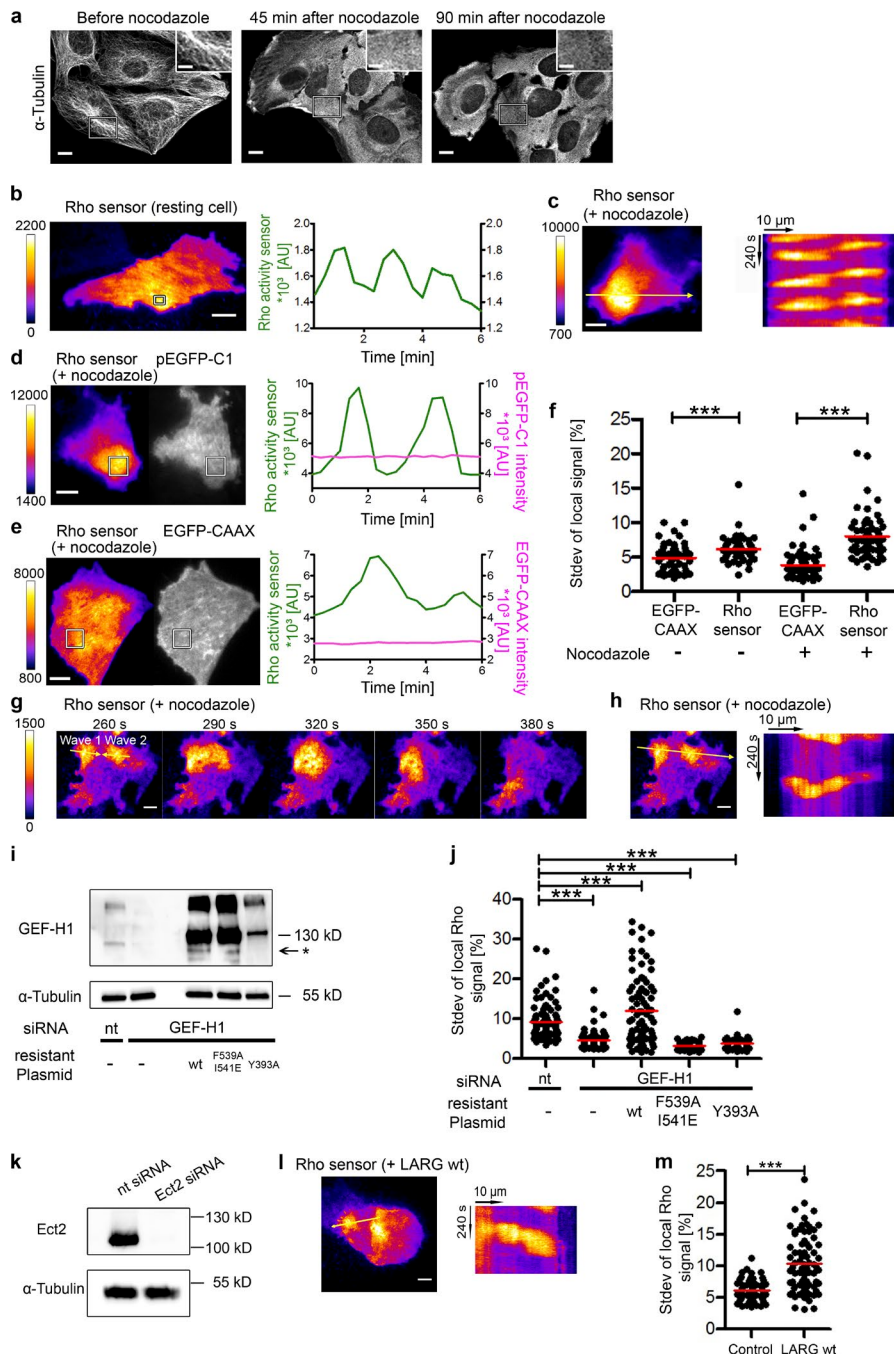


Figure S2. Characterization of Rho activity and plasma membrane association dynamics. (a) Representative maximal projections of confocal z stacks of U2OS cells before and 45 and 90 min after treatment with 30 μ M nocodazole. The depolymerization of α -tubulin was visualized via immunostaining. (b, left) Representative TIRF image of pulsatile Rho activity in nontreated, resting cells. (b, right) Rho activity signal within the box in the left panel. (c, left) Representative TIRF image of Rho activity waves after nocodazole treatment. (c, right) Kymograph corresponding to the white arrow in the left panel. (d and e) Direct comparison of Rho sensor and cytosolic (d) or plasma membrane–anchored (e) control sensor signals in the presence of nocodazole. Representative TIRF images of cells coexpressing Rho and control sensors (left). Raw profiles of fluorescence signals measured within white boxes in left panels (right). (f) Standard deviation of local Rho activity signal dynamics compared with membrane dynamics visualized by EGFP fused to a KRas-derived plasma membrane anchor (EGFP-CAAX; $n \geq 55$ cells from four experiments). (g and h) Annihilation of two colliding Rho activity waves in U2OS cells expressing the Rho activity sensor and GEF-H1 WT. (g, left) First frame of the time sequence. (h, right) Kymograph corresponding to white arrow in the left panel. (i) Representative Western blot of GEF-H1 rescue experiment. The knockdown efficiency was $78.9 \pm 7.3\%$ (mean \pm SEM; $n = 5$ experiments). The star denotes a band that migrates at lower molecular weight than the endogenous protein. This band presumably corresponds to a breakdown product of the overexpressed WT or F539A/I541E mutant. (j) Standard deviation of local Rho activity signal in cells treated with nocodazole and nt or GEF-H1 siRNA and coexpressing control (EGFP), siRNA-resistant GEF-H1 WT, siRNA-resistant GEF-H1 F539A/I541E, or siRNA-resistant GEF-H1 Y393A ($n \geq 71$ cells from three experiments). (k) Representative Western blot of Ect2 siRNA knockdown. The knockdown efficiency was $99.5 \pm 0.1\%$ (mean \pm SEM; $n = 3$ experiments). (l, left) Representative TIRF image of Rho activity in U2OS cells expressing the Rho activity sensor and LARG WT (GFP-LARG). (l, right) Kymograph corresponding to the arrow in the left panel. (m) Standard deviation of local Rho activity signal dynamics. Frame rate is 3/min (b–f, i, l, and m) or 20/min (g and h). Bars: (main) 10 μ m; (a, insets) 5 μ m. ***, $P < 0.001$ (f and m, unpaired t test; j, analysis of variance, Dunnett's post-test).

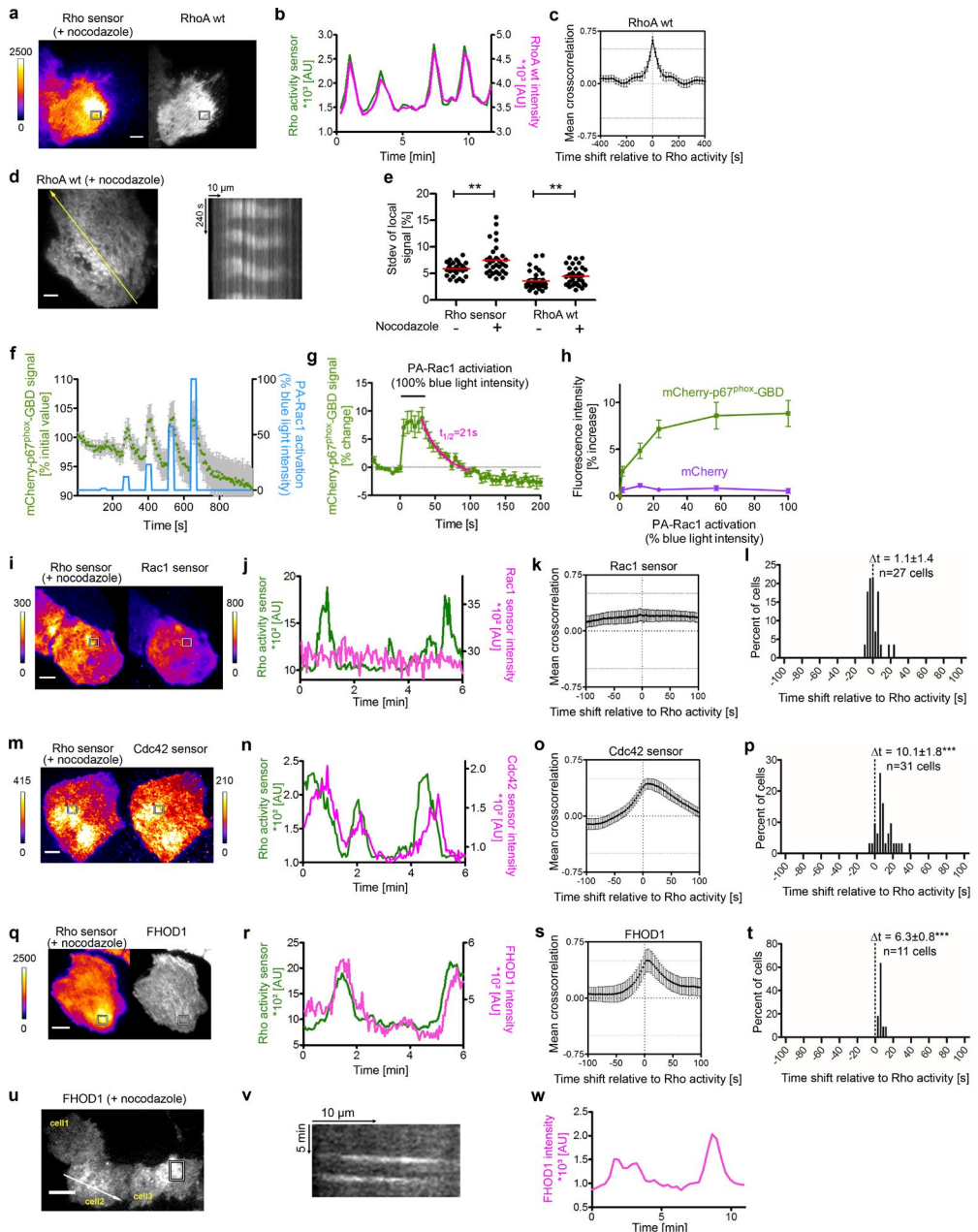


Figure S3. Local Rho activity pulses correlate with spatio-temporal patterns of RhoA and FHOD1 localization and Cdc42, but not Rac1 activity. (a–c) Pulses of Rho activity coincide with RhoA plasma membrane association. (a) Representative TIRF images of nocodazole-treated U2OS cells expressing the Rho-kinin-GBD-based Rho activity sensor and RhoA WT (GFP-RhoA). (b) Intensity measurements within the box in a. (c) Temporal cross-correlation function ($n \geq 35$ cells from three experiments; error bars represent 95% confidence interval). (d, left) Representative TIRF image of RhoA plasma membrane association waves in nocodazole-treated U2OS cells expressing RhoA WT (GFP-RhoA). (d, right) Kymograph corresponding to the yellow arrow in the left panel (e) Standard deviation of local Rho activity signal and WT RhoA (GFP-RhoA) plasma membrane association dynamics in cells before and after nocodazole treatment ($n \geq 35$ cells from three experiments). (f–h) A Rac1 construct that can be activated by blue light (PA-Rac1; Wu et al., 2009) was used to characterize the newly developed Rac1 sensor ($n \geq 11$ cells from three experiments). Specifically, Rac1 activity was controlled in HeLa cells by applying sequential pulses of blue light (422–432 nm), each with duration of 30 s and increasing light intensity. (f) mCherry-p67^{phox}-GBD based Rac1 sensor responses to Rac1 activity pulses. (g) Kinetics of the sensor response to full PA-Rac1 activation. The light-sensitive WT LOV2 domain in PA-Rac1 is activated by blue light very rapidly (within milliseconds; Wu et al., 2009). Dark state reversal is much slower (in the order of tens of seconds; Wu et al., 2009). The observed recruitment and release kinetics of the Rac1 sensor are within the range of those previous measurements and thus appear to predominantly represent the light-controlled PA-Rac1 activation and inactivation kinetics. (h) Dependence of Rac1 sensor signal on blue light activation intensity. No light-dependent signal change was observed for mCherry lacking the GBD domain, which acts as a control sensor. (i–l) Temporal cross-correlation analysis of the Rho activity sensor (mCherry-Rho-kinin-GBD or EGFP-Rho-kinin-GBD) and Rac1 activity sensor (mCherry-p67^{phox}-GBD; i–l), Cdc42 activity sensor (mCherry-WASP-GBD; m–p), or plasma membrane localization of WT FHOD1 (EGFP-FHOD1 WT; q–t) in nocodazole-treated U2OS cells. (i, m, and q) TIRF images. (j, n, and r) Intensity measurements within boxes in i, m, and q. (k, l, o, p, s, and t) Temporal cross-correlation functions (k, o, and s) and frequency distribution of cross-correlation maxima derived from k, o, and s (l, p, and t; $n \geq 11$ cells from at least three experiments; error bars: 95% confidence interval). (u) TIRF images of EGFP-FHOD1 in three representative BAC-transgenic mouse embryonic stem cells after nocodazole treatment. (v) Kymograph corresponding to the arrow in u. (w) Intensity measurements within the box in u. Frame rate is 20/min (a–e and i–t), 12/min (f–h), or 3/min (u–w). Bars, 10 μ m. **, $P < 0.01$; ***, $P < 0.001$ (e, paired t tests; l, p, and t, one-sample t test).

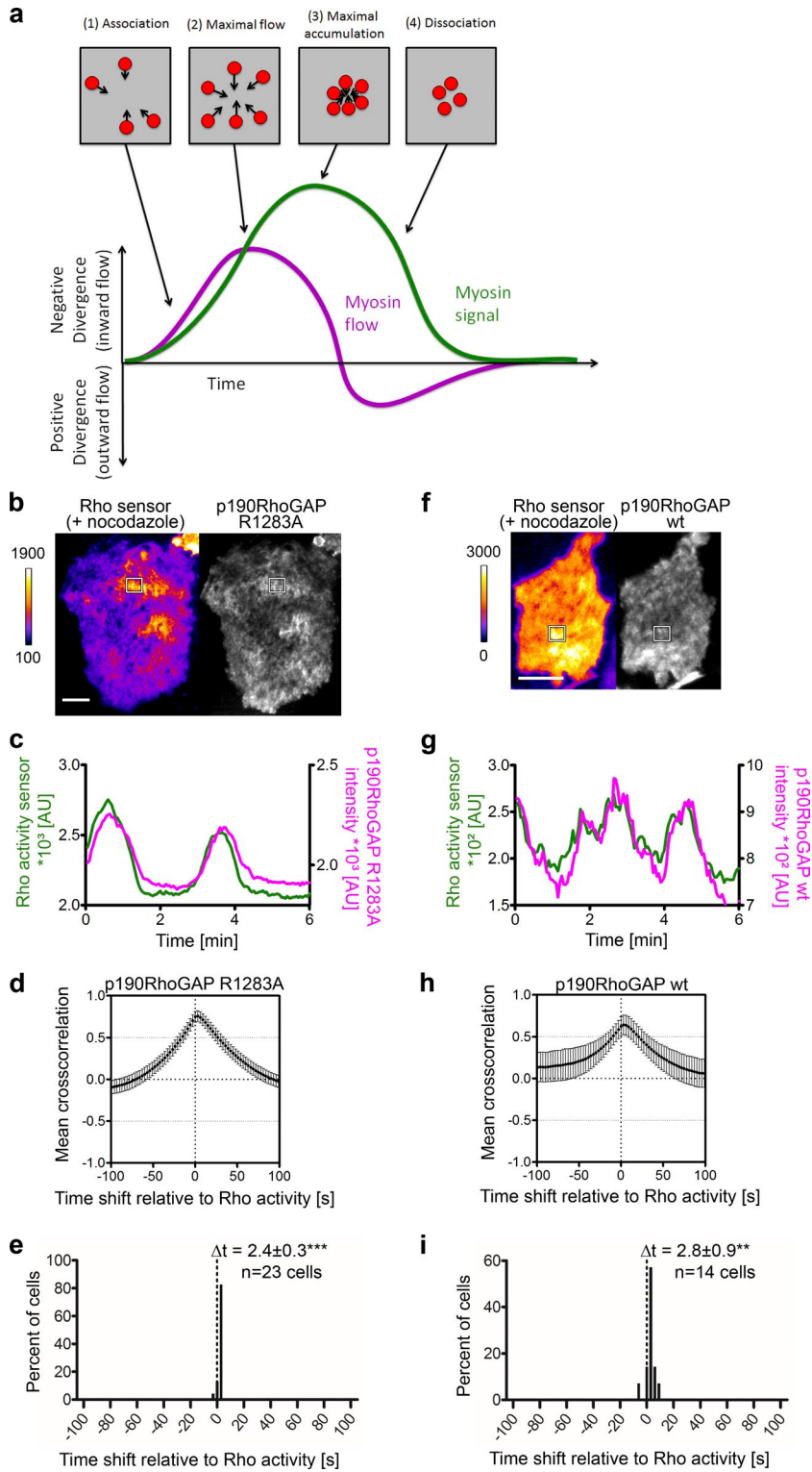


Figure S4. Characterization of actomyosin mediated cell contraction and Rho GAP recruitment. (a) Schematic representation of dynamic formation of contractile nodes. (1) Active myosin minifilaments associate with cortical actin and start to form a node with contractile flow directed to its center. (2) This contractile flow is maximal if the majority of myosin minifilaments move toward the node center. (3) Myosin is maximally concentrated if the majority of myosin minifilaments reached the node center. The mobility of myosin minifilaments decreases while they approach their destination in the node center. Thus, the contractile flow drops during this phase. This effect is accentuated if the node center becomes smaller than the resolution of the grid used for flow analysis. (4) Because of the slow turnover of actomyosin structures, the dissociation of myosin is further delayed. In some cases, this is accompanied with measurement of an outward flow of actomyosin (i.e., positive divergence or negative contractile flow; see also left y axis in Fig. 3 p). (b–i) Temporal cross-correlation analysis of the Rho activity sensor mCherry-Rhotekin-GBD and GAP-deficient (b–e) or WT p190RhoGAP (f–i) in nocodazole-treated U2OS cells. (b and f) TIRF images. (c and g) Intensity measurements within white boxes in panels b and f. (d, e, h, and i) Temporal cross-correlation (d and h) functions and frequency distribution of cross-correlation maxima (e and i) derived from panels d and h ($n \geq 14$ cells from at least three experiments; error bars represent 95% confidence interval). Frame rate is 20/min. Bars, 10 μ m. **, $P < 0.01$; ***, $P < 0.001$ (e and i, one-sample t test).

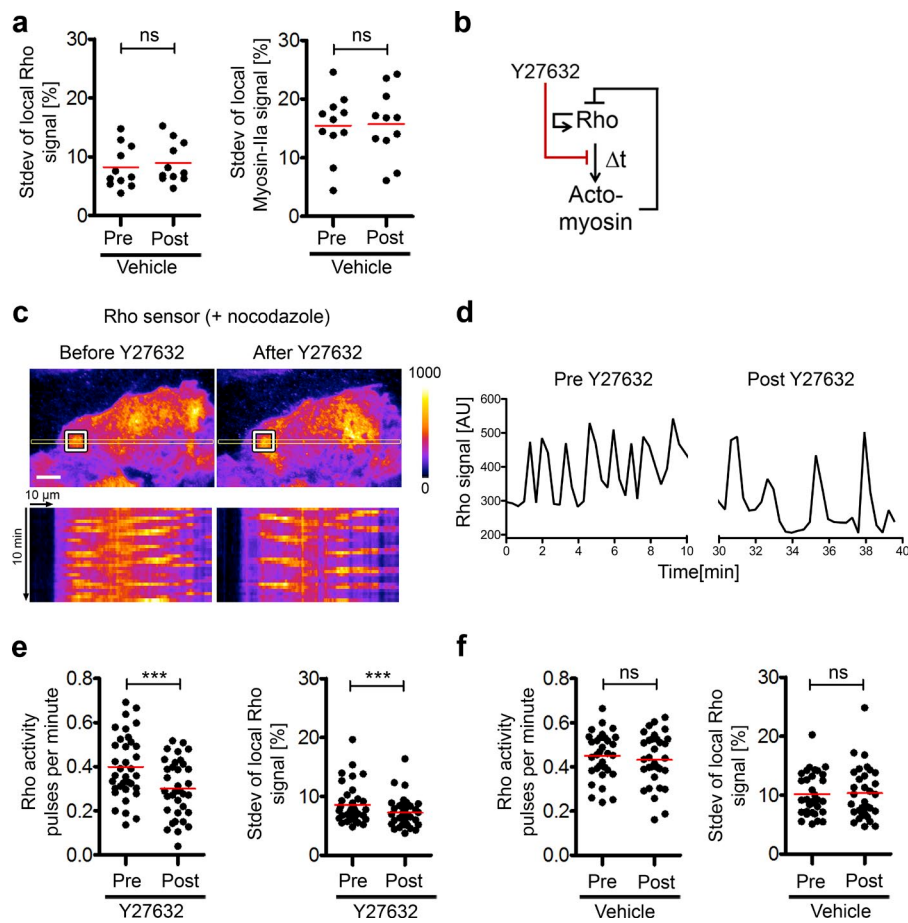
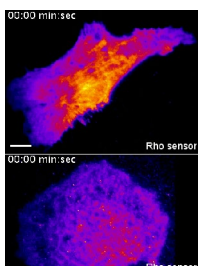
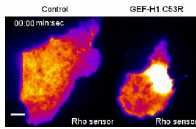


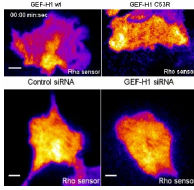
Figure S5. The Rho effector ROCK acts both downstream and upstream of Rho activity patterns in U2OS cells. (a) Standard deviation of local Rho and Myosin IIa signal in nocodazole-treated U2OS cells (vehicle-treated control cells for blebbistatin treatment shown in Fig. 5 (h and i); $n = 11$ cells from three experiments). (b) Schematics of proposed Rho activity-based excitable network and inhibition by the ROCK inhibitor Y27632. (c) TIRF images of the Rho activity sensor mCherry-Rhotekin-GBD after nocodazole treatment and before and after treatment with 50 μ M Y27632 (30 min). Kymographs correspond to yellow regions. (d) Intensity measurements within white regions indicated in c. (e and f) Frequency and standard deviation of the local Rho signal ($n = 35$ cells from four experiments for e and $n = 29$ cells from two experiments for f). Frame rate is 3/min. Bars, 10 μ m. ns, $P > 0.05$; ***, $P < 0.001$ (a, e, and f, paired t test).



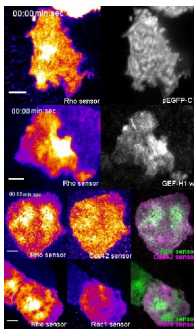
Video 1. Irregular pulses of Rho activity in resting U2OS cells and their stimulation by nocodazole treatment. Time-lapse TIRF videos of the Rho activity sensor mCherry-Rhotekin-GBD in representative U2OS cells. (Top) Resting U2OS cell. (Bottom) U2OS cell before and after 45- to 90-min treatment with 30 μ M nocodazole. Imaging started 48 h after plating on collagen-coated glass-bottom dishes. Images were collected with a frame rate of 3/min. Bars, 10 μ m.



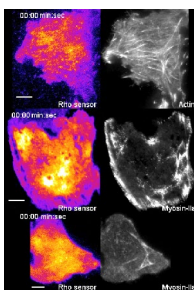
Video 2. Expression of active GEF-H1 C53R increases Rho activity pulse amplitude and wave propagation. Time-lapse TIRF videos of the Rho activity sensor mCherry-Rhotekin-GBD with EGFP (control, left) or in combination with active GEF-H1 (EGFP-GEF-H1 C53R, right) in representative U2OS cells. Images were collected with a frame rate of 3/min. Bars, 10 μ m.



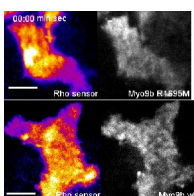
Video 3. GEF-H1 induces the formation of pulses and traveling waves of Rho activity and is required for Rho activity pulses in resting cells. (Top) Time-lapse TIRF videos of the Rho activity sensor mCherry-Rhotekin-GBD in combination with EGFP-GEF-H1 WT (left) or in combination with EGFP-GEF-H1 C53R (right) in representative U2OS cells. Images were collected 45–90 min after treatment with 30 μ M nocodazole using a frame rate of 20/min. Bars, 10 μ m. (Bottom) Time-lapse TIRF videos of the Rho activity sensor mCherry-Rhotekin-GBD in representative U2OS cells treated with nontargeting (nt; left) or GEF-H1 siRNA (right). Images were collected using a frame rate of 3/min. Bar, 10 μ m.



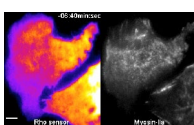
Video 4. Local Rho activity pulses do not correlate with EGFP or Rac1 activity signals but correlate with Cdc42 activity and GEF-H1 localization. (Row 1) Time-lapse TIRF video of the Rho activity sensor mCherry-Rhotekin-GBD (left) and EGFP (control sensor, right) in a representative U2OS cell. (Row 2) Time-lapse TIRF video of the Rho activity sensor mCherry-Rhotekin-GBD (left) and EGFP-GEF-H1 WT (right) in a representative U2OS cell. (Row 3) Time-lapse TIRF video of the Rho activity sensor EGFP-Rhotekin-GBD (left) and the Cdc42 activity sensor mCherry-WASP-GBD (middle) and overlay of both movies (right) in green (EGFP-Rhotekin-GBD) and magenta (mCherry-WASP-GBD) in a representative U2OS cell. (Row 4) Time-lapse TIRF video of the Rho activity sensor EGFP-Rhotekin-GBD (left) and the Rac1 activity sensor mCherry-p67phox-GBD (middle) and overlay of both movies (right) in green (EGFP-Rhotekin-GBD) and magenta (mCherry-p67phox-GBD) in a representative U2OS cell. Images were collected 45–90 min after treatment with 30 μ M nocodazole using a frame rate of 20/min. Bars, 10 μ m.



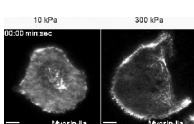
Video 5. Local Rho activity peaks precede maximal actin and Myosin IIa accumulation. (Top) Time-lapse TIRF video of the Rho activity sensor mCherry-Rhotekin-GBD (left) and EGFP-actin (right) in a representative U2OS cell. (Middle and bottom) Time-lapse TIRF video of the Rho activity sensor mCherry-Rhotekin-GBD (left) and Myosin IIa (EGFP-NMHCIIa, right) in a representative U2OS cell. Bottom panels show untreated, resting cells; images in the upper and middle panels were collected 45–90 min after treatment with 30 μ M nocodazole using a frame rate of 20/min. Bars, 10 μ m.



Video 6. Local Rho activity pulses are modulated by the RhoGAP Myo9b. (Top) Time-lapse TIRF video of the Rho activity sensor mCherry-Rhotekin-GBD (left) and a GAP-deficient mutant of the RhoGAP Myo9b (EGFP-Myo9b-R1695M, right) in a representative U2OS cell. (Bottom) Time-lapse TIRF video of the Rho activity sensor mCherry-Rhotekin-GBD (left) and WT Myo9b (EGFP-Myo9b-WT, right) in a representative U2OS cell. Images were collected 45–90 min after treatment with 30 μ M nocodazole using a frame rate of 20/min. Bars, 10 μ m.



Video 7. Myosin IIa acts both downstream and upstream of Rho activity patterns. Time-lapse TIRF video of the Rho activity sensor mCherry-Rhotekin-GBD (left) and Myosin IIa (EGFP-NMHCIIa, right) in a representative U2OS cell before and 60 min after treatment with 50 μ M of the Myosin II inhibitor blebbistatin. Images were collected 30–100 min after treatment with 30 μ M nocodazole using a frame rate of 3/min. Bar, 10 μ m.



Video 8. Modulation of cellular contractility signaling by matrix elasticity. Time-lapse videos of Myosin IIa (EGFP-NMHCIIa) in resting, untreated U2OS cells 12 h after plating on collagen-coated gel substrates with an elasticity of 10 kPa (left) or 300 kPa (right). Images were collected via spinning disk confocal microscopy using a frame rate of 20/min. Bars, 10 μ m.

Reference

Wu, Y.I., D. Frey, O.I. Lungu, A. Jaehrig, I. Schlichting, B. Kuhlman, and K.M. Hahn. 2009. A genetically encoded photoactivatable Rac controls the motility of living cells. *Nature*. 461:104–108. <https://doi.org/10.1038/nature08241>